

Project Number: 766719

Start Date of Project: 2017/11/01

Duration: 36 months

Deliverable 3.2 – V1.0**Title: Report on simulation platform for carrier relaxation dynamics and material gain, experimentally calibrated and validated to be used to feed design tools for QCL optimization**

Dissemination level	Public
Submission Date	2019/10/31
Work Package	WP3
Task	T3.2-T3.3
Type	Report
Version	1.0
Author	Luca Persichetti, Monica De Seta
Reviewed by	Michele Virgilio
Approved by (CO)	Monica De Seta

Disclaimer

The content of this deliverable does not reflect the official opinion of the European Union. Responsibility for the information and views expressed herein lies entirely with the author(s).

Table of Contents

Table of Contents	2
1. Forewords	2
2. The simulation platform.....	3
3. Relaxation dynamics in test MQW 3-level systems	11
4. Experimental calibration of the model	18

1. Forewords

This task is aimed at developing a simulation platform for carrier relaxation dynamics and material gain in optically excited multi-quantum well (MQW) structures, experimentally calibrated and validated, to be used to feed design tools for quantum cascade laser (QCL) optimization. Through this report, the simulation platform developed will be disclosed publicly.

A solid knowledge of carrier radiative and non-radiative dynamics is key to being able to estimate the material gain achievable with optically and electrically pumped quantum cascade (QC) emitters and it is the leverage for building up consistent quantum transport modeling and assessing optical gain of the full QCL devices developed in WP5. Since an electrically pumped Ge/SiGe QCL has been designed but not realized yet [1-3], the study of intersubband transition (ISBT) carrier dynamics under optical pumping may offer an easier experimental test bench to assess the performances of models of the out-of-equilibrium intersubband population dynamics. A numerical quantum model that has been experimentally verified on a SiGe MQW system under optical pumping can be very useful to understand the advantages and the limits of SiGe heterostructures also with respect to electrically pumped devices. To this end, the partners of the consortium (UNIROMA3, NEXTNANO, ETH, UGLA) developed in this task a self-consistent energy balance model, based on a rate equation approach, for intersubband carrier relaxation dynamics after pulsed optical excitation in MQW structures. The model features subband-dependent electronic temperatures and chemical potentials and includes elastic and inelastic scattering channels. The model has been calibrated on the basis of experimental data collected in task 3.2 on coupled MQWs which resemble the typical active-layer structure of the proposed Ge/SiGe QCL and on isolated MQWs systems. The investigated samples have been grown at UNIROMA3. The experiments performed to validate the model have been carried out at the free-electron laser (FEL) facility FELBE at Helmholtz Zentrum Dresden Rossendorf via proposal submissions and consist of:

- Terahertz (THz) absorption-saturation experiments where we measured the fluence-dependent transmittance of coupled MQWs under optical pumping of the 1->3 ISBT and its

numerical counterpart developed in this task 3.3. Experimental results and modeling are consistent, and both indicate absorption-saturation by ISBTs.

- THz photoluminescence (PL) experiments where we directly measured spontaneous photon emission from ISBTs of coupled MQWs under FEL optical pumping. We observed a PL peak at 4 THz, which can be attributed to the 3->2 and 2->1 ISBTs. The ISBT PL efficiency observed is in reasonable agreement with what expected in the model from the non-radiative/radiative lifetime ratio.
- Degenerate THz pump-probe spectroscopy to estimate relaxation lifetimes on isolated and coupled MQWs. The experimental results were compared to those of the numerical model to evaluate the dependence of excited state lifetimes on the MQW design, the degree of spatial overlap of electronic wavefunctions and energy level separation.

Through the calibration of the model, we obtained accurate values for material parameters which control the relevant electron scattering channels. These data have been transferred to the NEXTNANO platform in order to perform realistic quantum transport and gain calculations of Ge/SiGe THz QCLs using the nonequilibrium Green's function method.

2. The simulation platform

The simulation platform developed between M1 and M24 is composed by two modules:

- Module 1: Calculation of electronic states and optical equilibrium properties through a self-consistent multivalley effective mass model based on a Schrödinger-Poisson solver.
- Module 2: Carrier relaxation dynamics after pulsed optical excitation.

Module 1

The first module was described in detail in the Deliverable 3.1. Being this document disclosed to the public, we believe, however, that it is useful to revise briefly here its main outputs.

As test bed, we consider a set of coupled MQW samples which have been grown in the UNIROMA3 reactor by chemical vapor deposition (CVD) and optically characterized by Fourier Transform infrared spectroscopy (FTIR). As shown in the inset of Fig. 1(a), the sample design features a wide n-doped Ge well of thickness w_L and a narrow undoped well of thickness $w_n=5$ nm (kept always fixed). The two wells are separated by a SiGe tunnel barrier of thickness b_t and Ge composition x_{Ge} . Both w_L and b_t have been varied in the experiment, while x_{Ge} has been set to 0.81 or 0.87, with the higher Ge composition describing the more pronounced SiGe intermixing for $b_t < 3$ nm. In the samples, the module composed by the two Ge wells and the SiGe barrier in between them has been repeated 20 times with 21 nm thick $\text{Si}_{0.20}\text{Ge}_{0.80}$ barriers separating the individual modules.

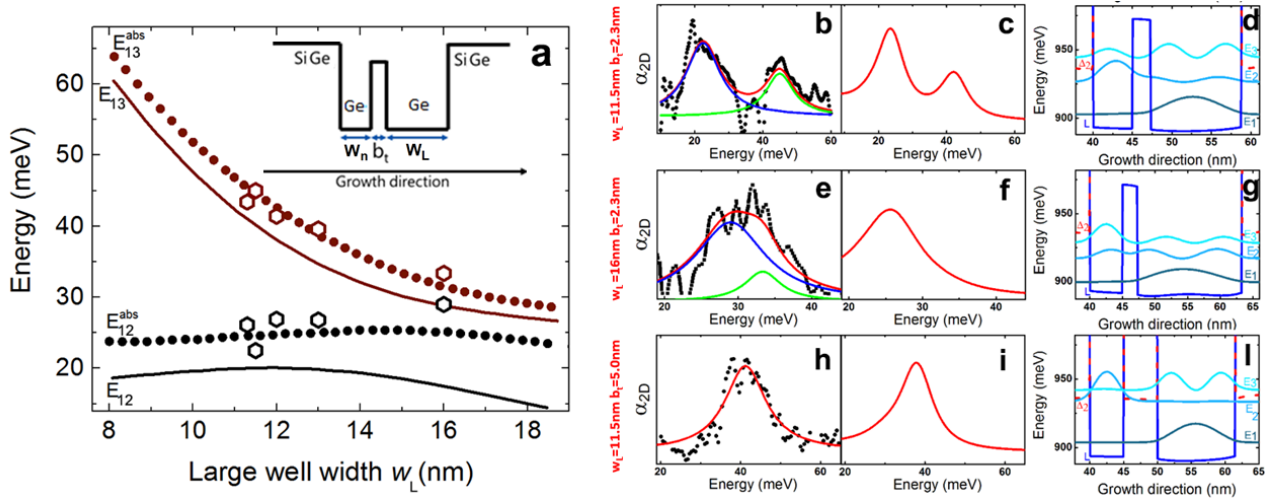


Fig. 1. (a) ISBT energies (continuous lines) and optical resonances (full dots) for asymmetric-coupled quantum well structures with a narrow well of 5 nm and a $\text{Si}_{0.15}\text{Ge}_{0.85}$ tunnel barrier $b_t = 2.3$ nm as a function of the wide well width w_L . The carrier density is $n_{2D} = 7 \times 10^{11} \text{ cm}^{-2}$. The empty dots represent experimental data points. The schematic structure of samples is shown in the inset of panel (a). Experimental (b, e, h) and calculated (c, f, i) optical absorption coefficients for samples featuring different w_L and b_t . The corresponding electron energies and squared wave functions for the relevant subbands are reported in panels (d, g, l).

The solid curves in Fig. 1(a) show the ISBT energies $E_{12} = E_2 - E_1$ and $E_{13} = E_3 - E_1$ between the fundamental (E_1), and, respectively, the first excited (E_2), and second excited (E_3) electron states of the asymmetric-coupled quantum well (ACQW) system described above when the wide well width w_L is varied at a fixed $b_t = 2.3$ nm. The positions of the related resonances expected in optical absorption spectra are shown as dotted lines and their energy difference with respect to the corresponding ISBT energy is due to the depolarization shift effect induced by a 2D free-electron density of $n_{2D} = 7 \times 10^{11} \text{ cm}^{-2}$ which is fully accounted in the model. The experimental optical absorption energies measured by FTIR are indicated by the empty hexagonal markers and will match the behavior predicted by the model. We also note that the minimum separation between E_{12} and E_{13} ISBTs is predicted to be around $w_L = 14$ nm which is the anticrossing point where, in the limit of non-interacting wells (i.e. large tunneling barrier), the E_2 and E_3 states would be resonant. The opening of a gap at the anticrossing reflects the hybridization between the ground state in the narrow well and the first-excited state in the wide well. The coupling of electron wavefunctions between the two wells can be controlled either by varying the width of the tunneling barrier (i.e. the central barrier thickness b_t) or by changing the relative alignment of confined L states of the two isolated wells (i.e. varying w_L for a fixed b_t).

In the first year of FLASH (Deliverable 3.1), we showed that we obtained a fine control over inter-well coupling and wavefunction tunneling by ACQW design. In the second year we grew new samples to complete this study investigating the limit of very large barrier thickness and the region where $w_L > 14$ nm, i.e. larger than the anticrossing point. We report some examples in Fig. 1(b-l). The panels (b) to (d) show, respectively, the experimental and calculated intersubband absorption spectrum α_{2D} and the electron energy and squared wavefunction for an ACQW system with $w_L = 11.5$ nm and $b_t = 2.3$ nm. Having been designed close to the anticrossing condition, this system is

characterized by a significant state hybridization which shows up in the appearance in the absorption spectra of the the E_{12} and E_{13} resonances with similar oscillator strengths. If now we design the system away from the anticrossing condition, increasing w_L to 16 nm (keeping b_t fixed) [Fig. 1(e-g)], it is clear that the optical resonance corresponding to the E_{12} ISBT becomes dominant in the measured and calculated absorption spectra (panels e and f). The oscillator strength of the E_{13} ISBT is in fact low, due to the fact the L_3 state is mainly localized in the thin well. By comparing panels g and d, it can be noticed that, for $w_L= 16$ nm, the E_2 and E_3 states are closer in energy compared to $w_L= 11.5$ nm, in line with panel (a); while the amplitude of the electron wavefunction of E_3 in the wide well, where the optical transition occurs, is higher for $w_L= 11.5$ nm (panel d), due to the stronger hybridization. The coupling of electron wavefunctions in the two wells can be also controlled by the width of the tunneling barrier (i.e. the central barrier thickness b_t). When the latter is increased from 2.3 to 5.0 nm [compare panels (b-d) and (h-l)] for a fixed $w_L= 11.5$ nm, a single optical resonance becomes dominant in the absorption spectra as observed in the experiment [panel (h)] and quantitatively predicted by the model [panel (i)]. By inspecting panel (l), it can be seen that, for the $b_t= 5.0$ nm - $w_L= 11.5$ nm design, the amplitude of the E_2 state is negligible in the wide well and, thus, the dominant optical transition occurs between the E_1 and E_3 states.

In summary, THz absorption spectroscopy measurements as a function of inter-well coupling in ACQWs allowed a careful validation of the equilibrium module of the simulation platform. We showed that the spatial overlap of electron wavefunctions can be finely controlled by design, allowing us to tune the diagonality of the ISBT matrix elements. In addition, the modeling accuracy in reproducing experimental intersubband absorption spectra guarantees high-precision design and reliability for the estimation of the L-point conduction-band offsets in the SiGe-heterostructure material system. This offset ultimately defines the tunneling barrier height. For our samples, we find a discontinuity of 117 meV for $x_{Ge} = 0.81$. This value is suitable for the development of an intersubband THz QCL laser.

Module 2

We have developed a carrier relaxation model for investigating intersubband systems with two [i.e. isolated MQWs Fig. 2(a)] and three levels [often referred to as quantum fountains, Fig. 2(b)] where free carriers are optically pumped from the ground state subband to an upper subband.

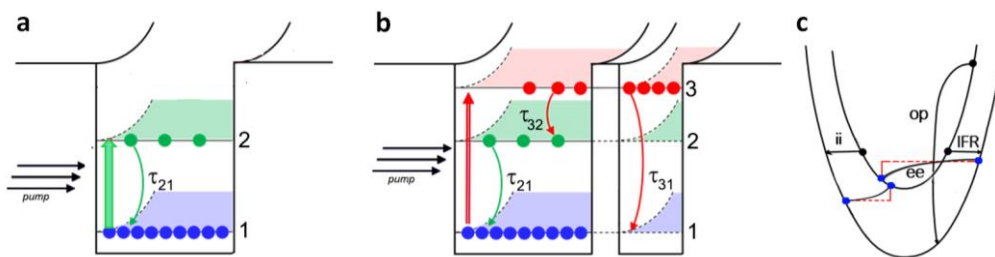


Fig. 2. (a, b) The relevant ISBTs and lifetimes in an isolated quantum well (panel a) and in a quantum fountain (panel b) under optical pumping. (c) Elastic and inelastic scattering mechanisms.

Among all non-radiative relaxation channels [sketched in Fig. 2(c)], the emission of optical phonon (OP) is the dominant inelastic scattering mechanism, since the intrasubband emission of acoustic phonons is characterized by very slow energy loss rates, typically of the order of hundreds of ps [4]. In addition to electron-phonon scattering, other sources of electron scattering must be taken into account for a proper description of the relaxation dynamics, such as the scattering by ionized impurity (II) atoms, the electron-electron (e-e) scattering or the interface roughness (IFR) scattering, the latter being critical in coupled well systems at the base of a QCL [Fig. 2(b)]. All these scattering channels are elastic and depend intimately on design/growth parameters, such as the doping concentration and the hetero-interface design and quality. An accurate model for simulating carrier relaxation dynamics with the inclusion of such elastic scattering channels was lacking till now. In literature, dynamical models are restricted only to the electron-phonon mechanism [5-7], whereas the models including all the channels do not consider them within a dynamic rate equation formulation including subband-dependent electronic temperatures [8]. Purpose of the simulation platform developed in task 3.3 and described by the present report paper is to fill such gap in the knowledge by addressing the role of both inelastic and elastic scattering mechanisms.

Dynamic model description

To describe the model we focus our attention on the three level dynamics of a *n*-type Ge/SiGe optically pumped quantum fountain. By exploiting Module 1, we first calculate by means of a multivalley effective mass Schrödinger-Poisson model the equilibrium electronic states at a given lattice temperature T^L . For each subband i with $i=1, 2, 3$, we evaluate the energy of the subband edge E_i^0 , the envelope wavefunction $\psi_i(z)$ and the 2D equilibrium carrier densities N_i , as resulting from the complete ionization of the donor states. When the system is optically excited via resonant pumping of the $1 \rightarrow j$ with $j > 1$ transition, the carriers are driven out of equilibrium and start to exchange energy with both the photon and phonon degree of freedom through intersubband and intrasubband scattering events, involving initial and final states belong to the same (intra-valley) or to different (inter-valley) degenerate L valleys. To describe the intersubband dynamics at the picosecond scale we assume, as suggested by Monte Carlo simulations [9], that the time dependent electron populations in all the subbands are at each time step instantaneously thermalized, due to the presence of fast intrasubband elastic scattering mechanisms. Under this hypothesis, the system is described by quasi-equilibrium Fermi distributions and we can define subband dependent electronic temperatures T_i^e and chemical potentials μ_i , which are treated as dynamical quantities in the model. Their values at each time step are evaluated as a function of $N_i(t)$ and $E_i(t)$ in order to fulfill the following equations:

$$(1) \quad N_i(t) = D \int_{E_i^0}^{\infty} \frac{dE}{1 + e^{(E-\mu_i)/k_B T_i^e}}$$

$$(2) \quad E_i(t) = D \int_{E_i^0}^{\infty} \frac{E dE}{1 + e^{(E-\mu_i)/k_B T_i^e}}$$

where E_i and N_i are the i -th subband energy and population, respectively; $D = 4m_d/(\pi\hbar^2)$ is the density of state (DOS) (with the inclusion of spin degeneracy) associated to the fourfold degenerate L valleys of Ge; m_d is the Ge in-plane dispersion mass calculated as $m_d = (m_1m_2)^{1/2}$ with $m_1 = m_t$ and $m_2 = (m_t + 2m_l)/3$ [10]; the longitudinal m_l and transverse m_t effective masses of Ge are reported in Table 1 together with the values adopted in our model for the other relevant material parameters.

Parameter	Description	Value
m_0	Electron mass	$9.10938291 \times 10^{-28}$ g
m_l	Longitudinal effective mass in Ge at L point	$1.59m_0$
m_t	Transverse effective mass in Ge at L point	$0.093m_0$
$1/M_{zz}$	Reciprocal of the inverse effective mass tensor matrix element zz (where z is the growth direction axis)	$0.13m_0$
Δ	RMS interface roughness amplitude from atomic probe tomography	0.18 nm
Δ_{eff}	Effective RMS interface roughness amplitude taking into account a finite vertical correlation among interfaces (See discussion in text)	0.11 nm
Λ	Interface roughness correlation length from atomic probe tomography	6.9 nm
$\hbar\omega_{eff}^{intra}$	Intravalley L-point optical phonon energy in Ge.	37.07 meV
$\hbar\omega_{eff}^{inter}$	Intervalley L-point optical phonon energy in Ge.	27.56 meV
Ξ_{OP}^{intra}	Intravalley effective deformation in Ge from Jacoboni et al. Ref. [11]	5.5×10^8 eV/cm
Ξ_{OP}^{inter}	Intervalley effective deformation in Ge from Jacoboni et al. Ref. [11]	3.0×10^8 eV/cm
$\Xi_{OP,eff}^{intra}$	Intravalley effective deformation in Ge estimated validating our model with pump&probe measurements	2.1×10^8 eV/cm

$\Xi_{OP,eff}^{inter}$

Intervalley effective deformation in Ge estimated validating our model with pump&probe measurements

0.25×10^8 eV/cm

Table 1. Relevant material parameters used in the model. Some of them have been estimated from the validation of the model with pump&probe experiments in MQW systems.

The dynamical evolution of subband populations and energies at each discrete time step are calculated starting from their equilibrium value at $t = -\infty$, solving the coupled differential equations which describe the energy and population time derivatives in terms of inter- and intra-subband scattering rates:

$$(3) \quad \begin{aligned} \frac{\partial}{\partial t} N_i = & \delta_{i,1} (W_{3 \rightarrow 1}^{pump} - W_{1 \rightarrow 3}^{pump}) + \delta_{i,3} (W_{1 \rightarrow 3}^{pump} - W_{3 \rightarrow 1}^{pump}) \\ & + \sum_{j \neq i} \sum_{intra,inter} (W_{j \rightarrow i}^{OP-} - W_{i \rightarrow j}^{OP-}) + \sum_{j \neq i} \sum_{intra,inter} (W_{j \rightarrow i}^{OP+} - W_{i \rightarrow j}^{OP+}) \\ & + \sum_{j \neq i} \left[(W_{j \rightarrow i}^{IFR} - W_{i \rightarrow j}^{IFR}) + (W_{j \rightarrow i}^{II} - W_{i \rightarrow j}^{II}) + (W_{j \rightarrow i}^{e-e} - W_{i \rightarrow j}^{e-e}) \right] \quad i, j = 1, 2, 3 \end{aligned}$$

$$(4) \quad \begin{aligned} \frac{\partial}{\partial t} E_i = & \delta_{i,1} (\overline{W}_{3 \rightarrow 1}^{pump} - \hbar\omega_p W_{3 \rightarrow 1}^{pump} - \overline{W}_{1 \rightarrow 3}^{pump}) + \delta_{i,3} (\overline{W}_{1 \rightarrow 3}^{pump} + \hbar\omega_p W_{1 \rightarrow 3}^{pump} - \overline{W}_{3 \rightarrow 1}^{pump}) \\ & + \sum_{j \neq i} \sum_{intra,inter} \left[(\overline{W}_{j \rightarrow i}^{OP-} + \hbar\omega_{eff} W_{j \rightarrow i}^{OP-} - \overline{W}_{i \rightarrow j}^{OP-}) + (\overline{W}_{j \rightarrow i}^{OP+} - \hbar\omega_{eff} W_{j \rightarrow i}^{OP+} - \overline{W}_{i \rightarrow j}^{OP+}) \right] \\ & + \sum_{intra,inter} \hbar\omega_{eff} (W_{i \rightarrow i}^{OP-} - W_{i \rightarrow i}^{OP+}) - \overline{W}_{i \rightarrow i}^{AC} \\ & + \sum_{j \neq i} \left[(\overline{W}_{j \rightarrow i}^{IFR} - \overline{W}_{i \rightarrow j}^{IFR}) + (\overline{W}_{j \rightarrow i}^{II} - \overline{W}_{i \rightarrow j}^{II}) + (\overline{W}_{j \rightarrow i}^{e-e} - \overline{W}_{i \rightarrow j}^{e-e}) \right] \quad i, j = 1, 2, 3. \end{aligned}$$

In the above equations, we considered the case of pumping the 1- \rightarrow 3 ISBT, the extension to the 1- \rightarrow 2 case is trivial. $W_{i \rightarrow j}$ and \overline{W}_{ij} represent particle and energy exchange rate per unit of surface due to scattering events associated to the perturbation potential specified in the superscript, where the initial state belongs to the subband i and the final state to subband j . We have considered IFR, interaction with II atoms and e-e scatterings as the relevant elastic processes, as detailed in the following. The inelastic mechanisms considered are the electron-photon interaction due to the pump beam (*pump*) and scatterings involving optical phonon absorption (*OP-*) and emission (*OP+*). In addition, intrasubband cooling by acoustic phonons (*AC*) can be also turned on in the calculations (See term $\overline{W}_{i \rightarrow i}^{AC}$ in Eq. 4), in case the timescale of the relaxation dynamics is longer than several hundreds of ps and, thus, the slow rate associated to the acoustic channel becomes relevant. This is not the case for the experimental data discussed in the following where the relaxation by *AC* will be therefore neglected. Note that, for the inelastic mechanisms, the energy transfer in Eq. 4 includes the energy exchanged with the involved photon ($\hbar\omega_p$) or phonon ($\hbar\omega_{eff}$). Moreover, in the above equation, only interactions with the phonon degree of freedom can

couple different degenerate L valleys, while the carrier interaction with the pump beam or the elastic scattering potential is limited to intra-valley processes due to the fast decay of the associated matrix element with the magnitude of the exchanged momentum. The rates $W_{i \rightarrow j}$ and \overline{W}_{ij} are calculated summing over all the initial and final states in subbands i and j taking into account the Fermi statistics. This summation can be expressed in terms of the initial energy according to:

$$(5a) \quad W_{i \rightarrow j} = D \int_{E_{min}}^{\infty} \frac{dE_i W_{i \rightarrow j}(E_i)}{1 + e^{(E_i - \mu_i)/k_B T_{e_i}}} \left(1 - \frac{1}{1 + e^{(E_j - \mu_j)/k_B T_{e_j}}} \right)$$

$$(5b) \quad \overline{W}_{i \rightarrow j} = D \int_{E_{min}}^{\infty} \frac{dE_i E_i W_{i \rightarrow j}(E_i)}{1 + e^{(E_i - \mu_i)/k_B T_{e_i}}} \left(1 - \frac{1}{1 + e^{(E_j - \mu_j)/k_B T_{e_j}}} \right)$$

where $E_j = E_i$ for elastic processes or $E_j = E_i \pm \hbar\omega$ when a photon or a phonon is absorbed/emitted. Energy conservation imposes for elastic scattering $E_{min} = \max(E_i^0, E_j^0)$, while for inelastic scattering $E_{min} = \max(E_i^0, E_j^0 \mp \hbar\omega_{eff})$, with the upper and lower sign referring to absorption and emission, respectively; E_i^0 indicates the energy minimum of subband i .

We now separately discuss in more details each scattering rate implemented in the model.

The instantaneous particle rate induced by the pump beam ($W_{i \rightarrow j}^{pump}$) with a beam of intensity $I(t)$, pump photon energy $\hbar\omega_p$ and propagation angle ϑ with respect to the growth direction in the MQW region, can be expressed in terms of the optical cross section σ through the following set of equations:

$$(6) \quad W_{i \rightarrow j}^{pump}(E_i) = \frac{\sigma I}{\hbar\omega_p \cos \theta}$$

$$(7) \quad \sigma = \frac{e^2 \pi \hbar}{2\epsilon_0 c n m_0} \left[\frac{(\Gamma/\pi) \cdot 2E_{ji}^0 \cdot 2\hbar\omega_p}{[(E_{ji}^0)^2 - (\hbar\omega_p)^2 + \Gamma^2]^2 + (2\hbar\omega_p \Gamma)^2} \right] \frac{\sum_{\gamma=1}^4 f_{ij}^{\gamma}}{4}$$

$$(8) \quad f_{ij}^{\gamma} = \frac{2m_0}{E_{ji}^0} (\hat{e}_x w_{xz}^{\gamma} + \hat{e}_y w_{yz}^{\gamma} + \hat{e}_z w_{zz}^{\gamma})^2 |p_{ij}^z|^2$$

The γ index runs over the four degenerate L valleys of Ge and the f_{ij}^{γ} terms represent the relative oscillator strengths calculated for the $i \rightarrow j$ transition. In Eq. (8), p_{ij}^z is the z component of the dipole matrix element, w_{ij}^{γ} are the components of the inverse mass tensor associated to valley γ and \hat{e} is the polarization vector of a linearly polarized beam propagating in the sample with the waveguide coupling geometry used [see Fig. 7(b)]. For the cross section in Eq. (7), a Lorentzian shape has been adopted to phenomenologically describe level broadening. Its half-width-at-half-maximum in the present report has been set to $\Gamma = 5$ meV, in line with recent experimental reports [12]. Notice also that in Eq. (7), the depolarization shift has been neglected since it is not expected to change the intersubband dynamics, and consequently the absorption resonance energy has been set equal to the bare intersubband transition energy $E_{ji}^0 = E_j^0 - E_i^0$. For the description of the temporal profile of the pump beam intensity $I(t)$, we use a Gaussian lineshape centered at $t = 0$ whose energy-dependent duration is chosen to reproduce the bandwidth-limited Gaussian pulses of the

FELBE. A full-width-at-half-maximum value of 5 ps is used consistent with the typical experimental values that are 13 (5) ps for the beam energy of 14 (29) meV typically used for pumping the 1-2 (1-3) ISBT [13].

OP scattering: Inelastic interaction of 2D electronic carriers with 3D optical phonons is evaluated assuming dispersionless branches of the vibrational modes at energies $\hbar\omega_{eff}$. The probability per unit of time for an electron in sub-band i to be scattered in subband j is expressed in terms of the modulus of the in-plane momentum $k_i=[2m(E_i-E_i^0)/\hbar]^{1/2}$ and is given by:

$$(9) \quad W_{i \rightarrow j}^{OP \mp}(k_i) = \frac{n_{dest} m_d \Xi_{OP}^2}{2\hbar^2 \rho \omega_{eff}} \left[N(\omega_{eff}, T^L) + \frac{1}{2} \mp \frac{1}{2} \right] F_{ij}$$

Ξ_{OP} is the effective deformation potential for the electron-phonon interaction, $N(\omega_{eff}, T^L)$ is the equilibrium Bose distribution for phonon energy $\hbar\omega_{eff}$ and lattice temperature T^L , $F_{ij} = \int dz \psi_j^2(z) \psi_i^2(z)$, with $\psi_i(z)$ and $\psi_j(z)$ being the envelope functions of the i -th and j -th state, respectively. The inter- and intra-valley scatterings are treated separately in the model, since in the former case larger values of exchanged momentum are involved. Thus, Ξ_{OP} and $\hbar\omega_{eff}$ differ in the two cases and their values are reported in Table 1. Also n_{dest} changes, since its value in eq. (9) specifies the number of different valleys for the final state, and it is therefore equal to 3 for inter-valley scattering while for intra-valley scattering $n_{dest} = 1$.

The scattering channels considered in the following are due to elastic processes, therefore the absolute value of the final momentum k_j for an allowed transition is fixed by energy conservation:

$$(10) \quad k_j = \sqrt{k_i^2 - \frac{2m_d}{\hbar^2} E_{ji}^0}, \quad E_{ji}^0 = E_j^0 - E_i^0$$

IFR scattering The impact of non-ideal heterointerfaces on the carrier dynamics is evaluated through a scattering rate depending on the interface roughness root-mean-square amplitude Δ , and correlation length Λ , which have been determined from the atomic probe tomography (APT) experiments in Task 3.1. Following Refs. [14,15], the IFR scattering rate for an electron in subband i with final state in subband j is defined as

$$(11) \quad W_{ij}^{IFR}(k_i) = \sum_{\mathcal{H}} \frac{|F_{ij,\mathcal{H}} \Delta \Lambda|^2 m_d}{\hbar^3} \int_0^\pi d\theta e^{-q_\alpha^2 \Lambda^2 / 4}$$

$$(12) \quad F_{ij,\mathcal{H}} = \int_{z_{\mathcal{H}}^-}^{z_{\mathcal{H}}^+} dz \psi_j^*(z) \frac{dV(z)}{dz} \psi_i(z)$$

In the first equation the sum extends over all the interfaces \mathcal{H} present in the system. Equation (12) gives the the strength of the coupling between initial and final states due to the band edge

potential $V(z)$ variation across the interface and $q_\alpha = k_j - k_i$ is the exchanged momentum in the scattering process [16].

Coulomb scattering The presence of the positively charged ions and other electrons also has a direct effect on the dynamics giving rise to elastic scatterings by a Coulomb (C) potential which depends on the density of positive ions and other electrons along the growth direction z . For the case of impurities, i.e. fixed ions infinitely heavy with respect to the electrons, this is given by the static concentration of dopants $n_{3D}(z)$ which is tailored to reproduce the typical spatial profile and broadening of donor concentration obtained from secondary ion mass spectrometry (SIMS) experiments (WP4). For the case of electrons, instead, a mean field approach is used to limit computational workload, i.e. the e-e interaction which is a two body process is thus reduced to a single particle scattering event. Each electron in a sub-band i is elastically scattered to the final sub-band $j \neq i$ interacting with the electron density ($|\psi_k(z_0)|^2$) of subbands $k=1,2,3$ at each point in the growth direction. We thus consider a generalized expression for the scattering rates due to Coulomb interactions where the II and the e-e contributions differ by their form factors:

$$(13) \quad W_{ij}^C(k_i) = \frac{m_d e^4}{4\pi \hbar^3 \epsilon^2} \int_0^\pi d\theta \frac{J_{ij}^{II}(q_\alpha) + \sum_k J_{ij,k}^{ee}(q_\alpha)}{(q_\alpha + q_{TF})^2}$$

$$(14) \quad J_{ij}^{II}(q_\alpha) = \int n_{3D}(z_0) \left(\int dz \psi_j^*(z) e^{-q_\alpha |z-z_0|} \psi_i(z) \right)^2 dz_0$$

$$(15) \quad J_{ij,k}^{ee}(q_\alpha) = \int n_k |\psi_k(z_0)|^2 \left(\int dz \psi_j^*(z) e^{-q_\alpha |z-z_0|} \psi_i(z) \right)^2 dz_0$$

where $q_{TF} = m_d e^2 / 2\pi \hbar^2 \epsilon$. Finally, the model features two different screening potentials, Thomas-Fermi and Debye, which can be used depending on the lattice temperature. The Thomas-Fermi screening is known to be a realistic approximation at low temperatures [17], and, since all the experimental data discussed in the following are acquired at $T < 10$ K, will be used hereinafter.

3. Relaxation dynamics in test MQW 3-level systems

As a test bed for the simulation platform and to illustrate its main features, we now apply the model described above to two coupled MQW systems which represent the more common design configurations for realizing a 3-level system: the tunnel barrier (TB) and the stepwise MQW architectures [Fig. 3(a, b)]. The asymmetry of both the structures enables ISBT between the ground and the second-excited states, L_1 and L_3 respectively, which are instead forbidden for symmetric quantum wells for parity reasons of the wavefunctions. Such asymmetry is realized in the TB design by two Ge wells of different widths separated by a $\text{Si}_{0.15}\text{Ge}_{0.85}$ TB [Fig. 3(a)]. The two wells and the TB are embedded within 21 nm thick $\text{Si}_{0.20}\text{Ge}_{0.80}$ layers. The TB design has been already introduced in Fig. 1 when discussing the equilibrium optical properties and, hereafter, we will use the same nomenclature as in Sect. 1 for describing its geometry. The second kind of

configuration [Fig. 3(b)] features a Ge well of width w_L and a $\text{Si}_{0.03}\text{Ge}_{0.97}$ step of width w_S embedded within 21 nm thick $\text{Si}_{0.20}\text{Ge}_{0.80}$ layers. This second strategy allows the configuration to be asymmetric without a tunneling barrier and is referred to as NTB. Having different number of hetero-interfaces, the TB e NTB structures allow us to highlight the impact of IFR on carrier relaxation dynamics in a 3-level system. The design parameters used for the two test configurations were selected so that the ISBT energies match between the two structures [Compare Figs. 3(a) and 3(b)]. This is quite important for comparing the dynamics of the two systems since OP scattering depends critically on the relative values of ISBT energy and phonon energies.

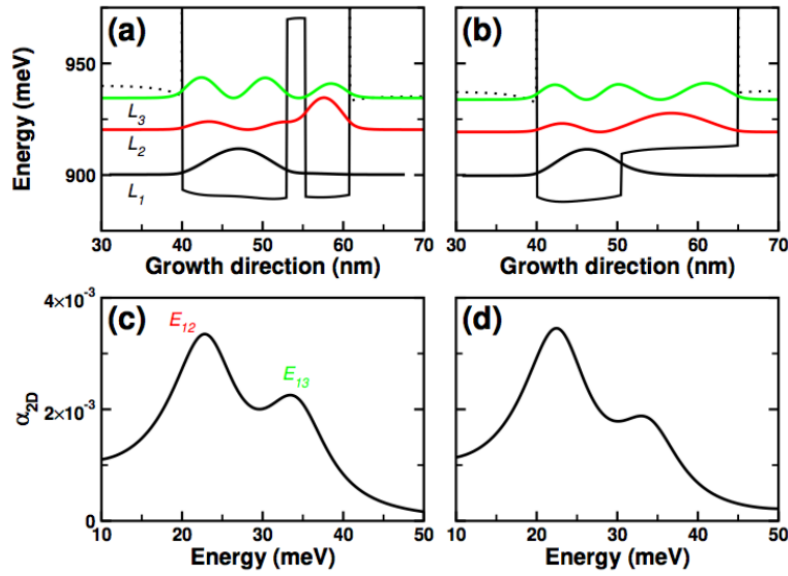


Fig. 3. Electron energy and squared wavefunction for (a) the tunneling barrier system (TB) and (b) the non-tunneling barrier system (NTB). Solid black curves represent the L band profiles. The electron population in the first confined state is $n_{2D} = 5 \times 10^{11} \text{ cm}^{-2}$ for both the systems. The two systems have been optimized in order to obtain similar absorption spectra reported in (c) and (d).

In addition, despite the structural difference, the two systems have been designed to have comparable optical absorption coefficients (α_{2D}) at the same doping level [Figs. 3(c) and 3(d)]. This is obtained by engineering the parameters of the systems so to achieve comparable $1 \rightarrow 2$ and $1 \rightarrow 3$ oscillator strengths.

The relaxation dynamics induced by a resonant $E_1 \rightarrow E_3$ pump is reported in Fig. 4, where populations and electronic temperatures are shown for the first three levels as function of the probe delay time with respect to the pump. The results are shown for the TB and NTB configurations and for two different doping levels, $n_{2D} = 5 \times 10^{10} \text{ cm}^{-2}$ (low doping, LD) and $n_{2D} = 5 \times 10^{11} \text{ cm}^{-2}$ (high doping, HD). The intensity of the pump is set to ensure a 2% peak population in L_3 for all configurations and is typically in the range of 0.5-1.3 kW/cm^2 .

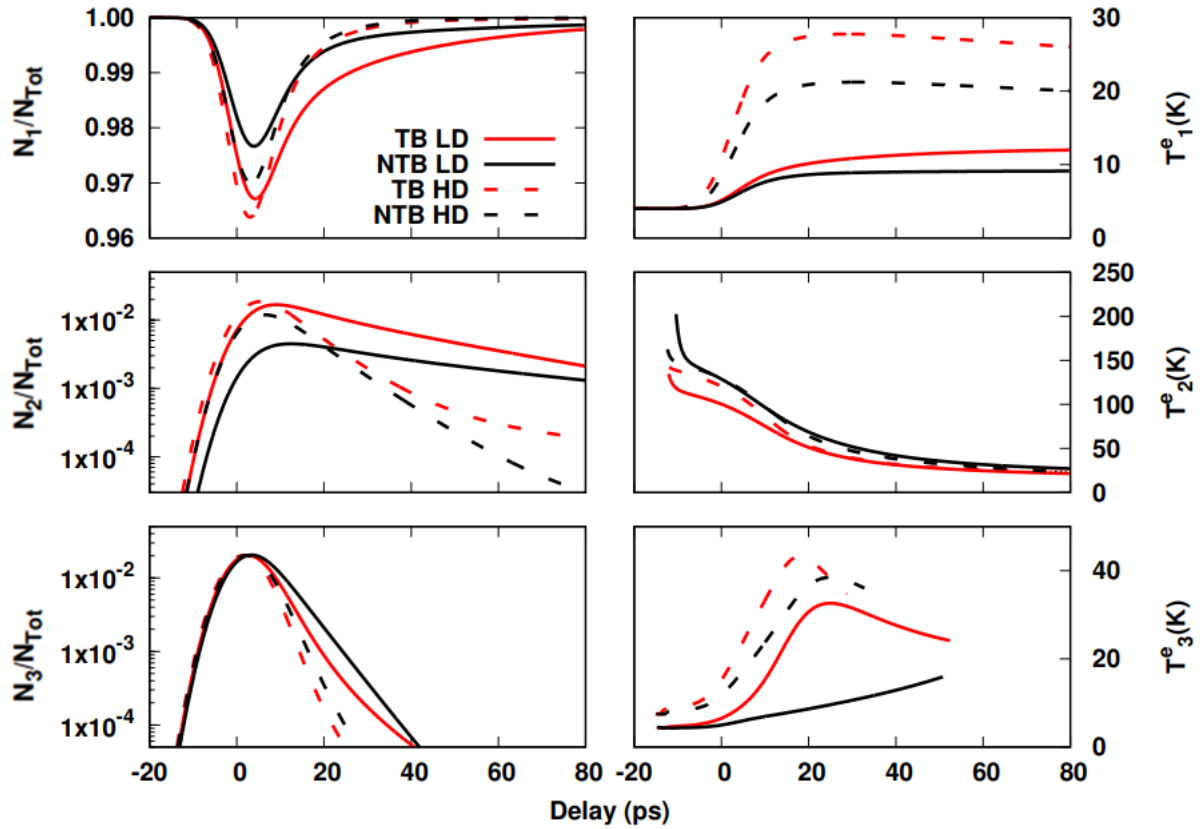


Fig. 4. Population dynamics at a lattice temperature of 4 K for the fundamental and the first two excited states (left column) and their electronic temperatures (right column) calculated for low doping (LD) concentration ($n_{2D} = 5 \times 10^{10} \text{ cm}^{-2}$) and high doping (HD) concentration ($n_{2D} = 5 \times 10^{11} \text{ cm}^{-2}$). For both the systems, the intensity of the pump is set to ensure a 2% peak population in L_3 . N_{tot} is the total number of electrons.

Although the relevance of OP scattering on the relaxation dynamics is well-known [4,7], any model for a $E_1 \rightarrow E_3$ pump-induced relaxation dynamics would be severely inaccurate without the inclusion of elastic scattering channels. In fact, for energy spacings $E_{32} < \hbar\omega_{eff}$ where $\hbar\omega_{eff} = 27.56$ meV for intervalley phonons and $\hbar\omega_{eff} = 37.07$ meV for intra-valley phonons [11] no electronic transitions from L_3 towards L_2 would be possible with the emission of optical phonons, unless thermally activated by a high electronic temperature of L_3 . Our model comprehensive of the elastic channels shows, on the contrary, that the L_2 population cannot be neglected, since the population N_2 reaches the same values as N_3 (See middle and bottom panels of Fig. 4). The filling of L_2 occurs via a two-step process $1 \xrightarrow{\text{pump}} 3 \xrightarrow{\text{elastic}} 2$, resulting in the short delay of a few picoseconds between the population peaks of L_2 and L_3 in Fig. 4. Elastic scatterings are *horizontal* transitions that allow only momentum exchange but conserve total energy. Thus, the $3 \xrightarrow{\text{elastic}} 2$ process brings hot electrons to level L_2 and, consequently, the electronic temperature of level 2 (T_2^e) exceeds 200 K. The long tail in the Fermi distribution arising from such a high T_2^e enables fast $2 \rightarrow 1$ ISBTs with optical phonon emission contributing to the rapid L_2 cooling rate that follows (middle panels of Fig. 4). In other words, an initial fast cooling stage of L_2 is followed by a slower one at longer delays, when the thermally activated emission of OPs in the $2 \rightarrow 1$ transition is

suspended. In general, for all the population dynamics shown in Fig. 4, the dominant relaxation mechanism of each level varies with the delay, depending on the specific electronic temperature and occupancy of that channel at a given time. Therefore, it is not possible to approximate the decay of the population dynamics with a single exponential behavior. By visual inspection of the population dynamics in Fig. 4, it is noteworthy that, at the same doping level, the relaxation for the NTB configuration is always slower than for the TB one. This is confirmed by Fig. 5(a) where we report, for the TB and NTB case, the non-net relaxation times, averaged over the 0-100 ps delay range, for the ISBT of interest as a function of n_{2D} . We remind that the non-net relaxation time τ_{ij} for the $i \rightarrow j$ scattering is related to the corresponding non-net rate W_{ij} by $\tau_{ij} = (W_{ij} / n_i)^{-1}$ where n_i is the electron population in the subband i . We notice that the difference between the TB and NTB case is particularly marked for the 3-2 and 2-1 transitions at low doping concentrations. For these transitions, the relatively small energy difference between the levels allows mostly elastic scatterings. Among them, the IFR channel is dominant at low values of n_{2D} , causing the difference in lifetimes between TB and NTB to be particularly large at low doping. This difference arises from the fact that the NTB design has one interface less (one less term in the summation showing up in equation 11). Moreover, the band-edge potential $V(z_H)$ at the interface has a lower amplitude for the NTB case [Compare Figs. 3(a) and 3(b)], giving a lower absolute value for $F_{ij,H}$ in Eq. 12. From equation 11, the strength of IFR scattering depends on the structural parameters Δ and Λ and, as said, by the factor $F_{ij,H}$. Since from Eq. 12 $F_{ij,H}$ depends on the amplitude of the envelope functions $\psi_i(z)$ and $\psi_j(z)$ at the interface, in the TB configuration we expect the $F_{ij,H}$ term (and, thus the IFR scattering rate) to be higher at larger penetrations of $\psi_i(z)$ and $\psi_j(z)$ in the barrier region. This is indeed verified in Fig. 5(b): From what we have discussed in sect. 2, the maximum penetration of the envelope functions in the barrier region occurs at the anticrossing point [12] where the hybridization of the isolated wave function from the separate sub-wells is the largest. For the TB configuration of Fig. 3(a), the anticrossing point is at $w_L \approx 140 - 150 \text{ \AA}$, where, as evident in the inset of Fig. 5(b), E_{32} has a minimum [12]. For the same w_L value, the net 3-2 transition rate associated to the IFR channel ($W_{32}^{IFR} - W_{23}^{IFR}$) is indeed maximum [Fig. 5(b)].

By comparing now the same structure (TB or NTB) at different doping levels in Fig. 4, we observe how, in the high-doping case, carrier dynamics is much more rapid. For instance, a decrease of N_2/N_{tot} of one order of magnitude takes >100 picoseconds for the low doping case while only 50 picoseconds in the high doping case. For the case of total ionization of the donors, implemented in the present model, the 3D donor concentration n_{3D} is a direct estimate of the sheet carrier density in the quantum well region (n_{2D}). Since n_{3D} enters the model in the equations of the Coulomb interactions in eq. 13-15, this gives a straightforward and expected dependence on doping concentration: Coulomb scattering will increase with increasing n_{2D} . Accordingly in Fig. 5(a), all the ISBT relaxation times reported become shorter at increasing doping levels and TB relaxation times are always smaller than the NTB ones, with a particularly marked difference for the 3-2 and 2-1 transitions at low doping concentrations where the relative weight of the IFR contribution is larger.

At high doping concentrations all lifetimes drop, and Coulomb scattering becomes dominant, hiding the effect of IFR described above: thus, TB and NTB curves converge.

The relaxation time τ_{31} reported in Fig. 5(a) is always shorter than all the other ISBT relaxation times reported, for any configuration at any doping level, indicating that the emission of optical phonons is indeed the most relevant scattering process for this transition. In fact, for both configurations and doping levels, E_{31} is in the range $\approx 31 - 33$ meV thus above the inter-valley OP and reachable by the intra-valley OP, considering the electronic temperatures of level L_3 being up to 40 K in the present calculations (Fig. 4). Thus, both inter- and intra-valley OP scattering channels are active, explaining the fast τ_{31} transition times obtained. To better elicit the dependence of the OP transition rates we report in Fig. 5(c) the dependence of the net 3-1 transition rate, both total and OP resolved, as a function of the E_{31} energy spacing for the high doping TB structure. The total rate follows the one associated with the OP channel alone when the inter-valley optical phonon energy is reached around 27 meV and increases monotonically with E_{31} .

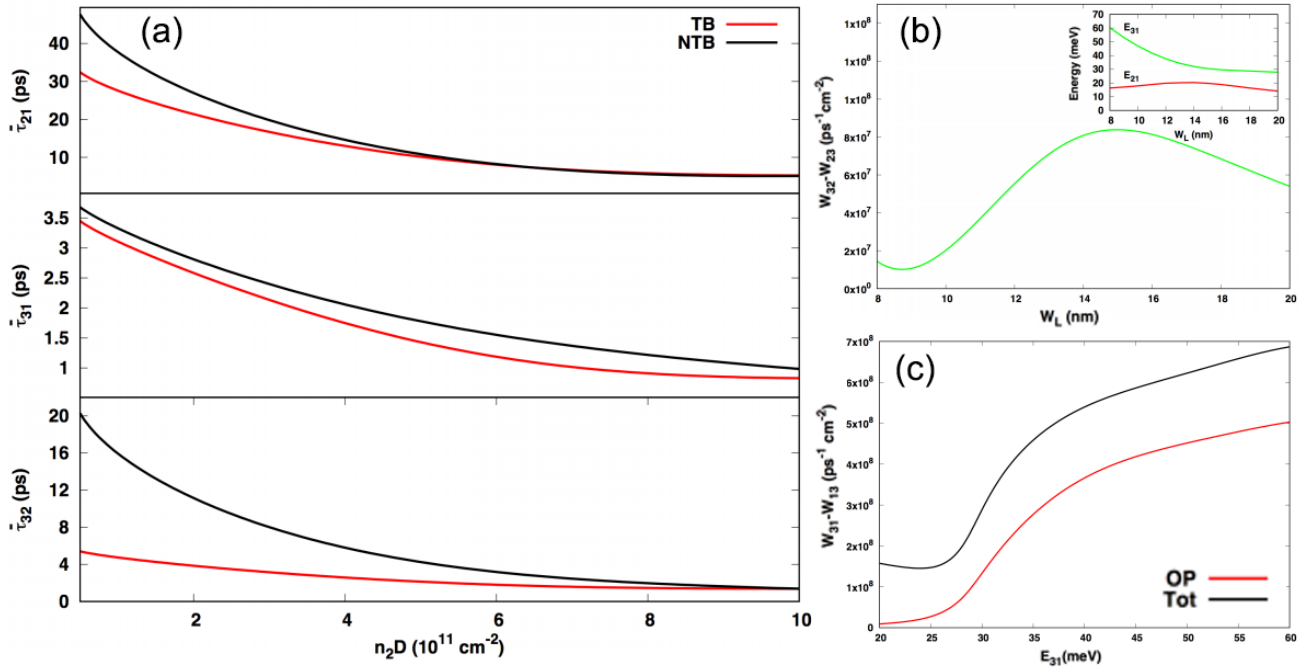


Fig. 5. (a) Non-net relaxation times as a function of the doping concentration n_{2D} for the TB and NTB systems (red and black curves, respectively). Since the population dynamics follows a non-single exponential behavior, the lifetimes have been averaged over the 0 – 100 ps delay range. For the highly doped TB configuration: (b) Net transition rate between L_2 and L_3 associated to the interface roughness channel as a function of the width of the wide quantum well w_L . In the inset the corresponding E_{31} and E_{21} transition energies are reported as a function of w_L . (c) Net transition rate between L_3 and L_1 associated to the optical phonon channel (red) and the sum of all the channels (black) as a function of the E_{31} transition energy.

Understanding the role of the different scattering channels on the population dynamics constitutes a key step towards a quantitative determination of the relevant physical parameters which ultimately drive population inversion and material gain. The population dynamics of the

different energy levels are determined by the total net transition rates between couples of energy levels $W_{ij}^{Tot} = W_{i \rightarrow j}^{Tot} - W_{j \rightarrow i}^{Tot}$ given by the sum of the various contributions of the single scattering channels. In Fig. 6, we thus resolve W_{ij}^{Tot} by scattering channel for each ISBT of the 3-level system, showing data for the TB and NTB configurations at high ($n_{2D} = 5 \times 10^{11} \text{ cm}^{-2}$) and low doping ($n_{2D} = 5 \times 10^{10} \text{ cm}^{-2}$). When scanning horizontally the panels comparing TB and NTB structures with same doping level, we notice that the IFR channel is the one changing most, as it could have been expected by the forgoing discussion. In particular, the $W_{2,3}^{IFR}$ is the rate that exhibits the biggest reduction, when reducing the number of interfaces. Since E_{32} is the lowest energy difference, the momentum exchange q_α required is smaller for the 3-2 ISBT, thus easing such process. While this reasoning is valid for any elastic scattering channel, for IFR we also notice that the integral in Eq. 12 is maximum when the highest energy level envelope functions are involved, being thus higher for $W_{2,3}^{IFR}$ with respect to IFR-assisted rates for other ij transitions.

By moving vertically in Fig. 6, we compare the same configuration, TB or NTB, at different doping levels. In general, all rates decrease with decreasing doping and we now focus on a relative comparison between the different channels at the same doping level for each ij transition. In both the high and low doping cases, at short delay times, i.e. when L_3 is strongly populated, optical phonons give the strongest contribution to W_{13}^{Tot} , as expected by the large E_{31} . More interesting is the case of the W_{12}^{Tot} rate which exhibits a completely different behavior: In fact only for the low doping case W_{12}^{OP} is the dominant contribution to the total net rate, while in the high doping case $W_{12}^C = W_{12}^{II} + W_{12}^{ee} > W_{12}^{OP}$. Moreover, at low doping, we notice that the optical phonon (OP) and Coulomb (C) curves cross each other, since W_{12}^{Tot} exhibits two distinct depletion stages as a function of the delay time. A first stage with a steeper W_{12}^{Tot} is dominated by the optical phonon channel and occurs within the initial delay range when $T_2^e > 50 \text{ K}$ in Fig. 4 and thus fast OP emission can occur from the tail of the Fermi distribution of electrons in L_2 towards L_1 . In a second stage, at longer delay times, a less steep W_{12}^{Tot} curve is observed. In this second stage L_2 has cooled down and optical phonons cannot be emitted anymore, thus the elastic Coulomb scattering becomes dominant and the overall total scattering rate W_{12}^{Tot} behavior follows the lower slope of the blue Coulomb curve. Already for $n_{2D} = 5 \times 10^{11} \text{ cm}^{-2}$ this double stage depletion for W_{12}^{Tot} is not observed anymore. For the high doping case, Coulomb scattering is always the highest one and the total scattering rate reproduces at any delay time the typical slope of the Coulomb curve.

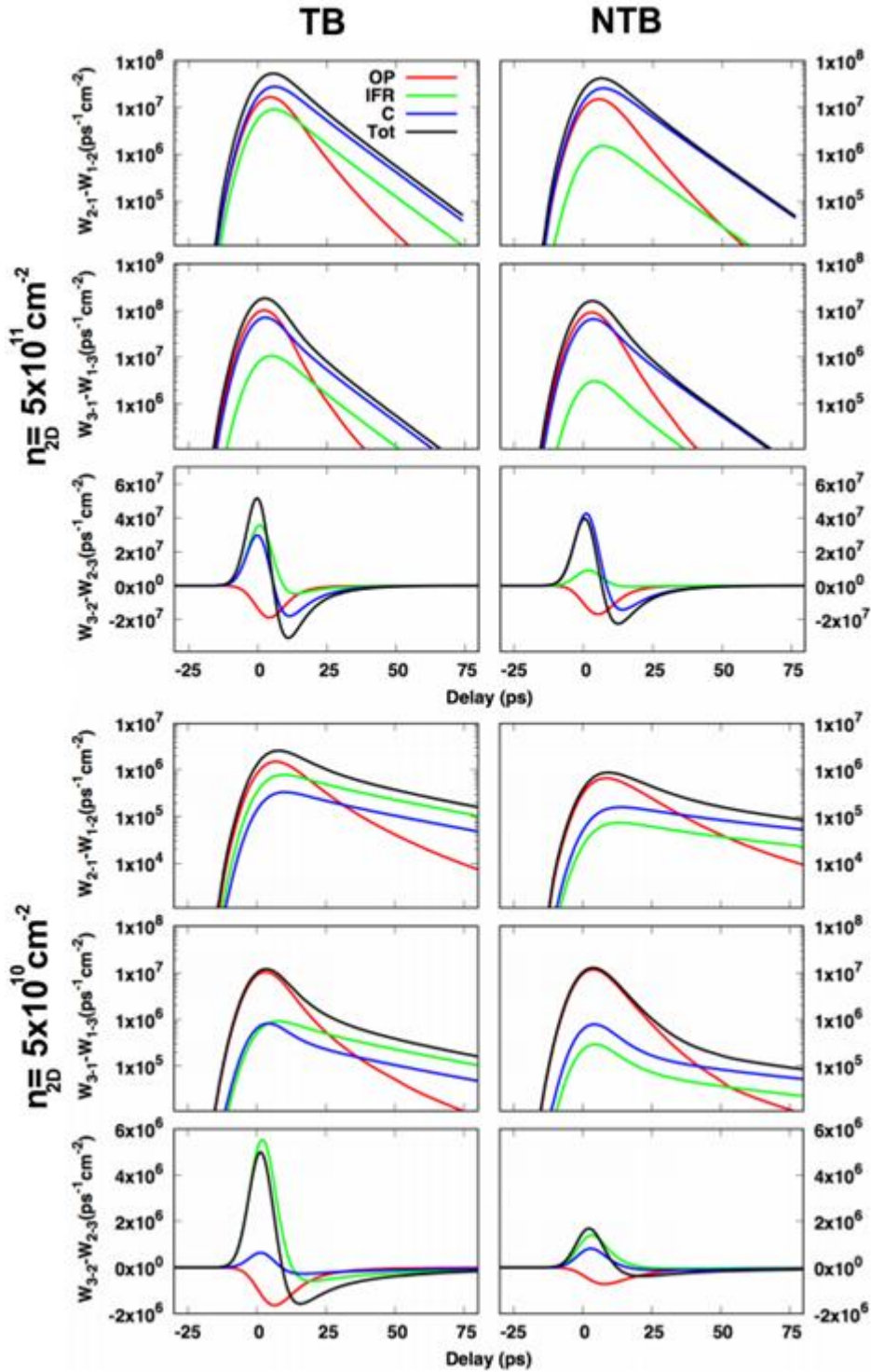


Fig. 6. Net transition rates between subbands i and j as a function of probe delay time resolved by scattering channel for the high (top panels) and low (bottom panels) doped samples: optical phonon (red curve), interface roughness (green curve), Coulomb (blue curve), and all the scattering channels summed (black curve). Left columns refers to the TB system, right column shows the results for the NTB configuration.

The rates discussed insofar are dominated by a *forward-scattering* $i \rightarrow j$ with $i > j$. The transitions between levels L_2 and L_3 behave differently. These processes are mostly caused by interface

roughness, due to the short energy distance of the two levels, but also an evident $2 \rightarrow 3$ *back-scattering* occurs, in particular for optical phonons, giving negative W_{23}^{OP} rates. This feature can be traced back to the high values of T_2^e (> 35 K, see Fig. 4), resulting in long tail distributions from which some electrons can scatter from L_2 to L_3 emitting optical phonons [18].

In summary, we have shown how the inclusion of elastic channels in the simulation of carrier relaxation dynamics allowed us to pinpoint a plethora of relaxation mechanisms, like back-scattering effects, which had been completely discarded from previous modelling approaches but constitute important pathways in the dynamics of 3-level systems. In the following section we will focus on some examples where the simulation platform has been applied for reproducing experimental data, thus allowing us a proper calibration and validation of the model.

4. Experimental calibration of the model

During Years 1 and 2 of FLASH, the consortium carried out two beamtime experiments at the FELBE facility in Dresden with the goal of collecting experimental data for the calibration and validation of the dynamic model described above.

In a first set of experiments, carried out in May 2018, the non-equilibrium optical properties of TB MQWs are studied by absorption-saturation measurements and compared to the numerical model of subband population dynamics after pulsed laser excitation described above. The preliminary analysis of these dataset was included in the Deliverable 3.1 which also included a full characterization of the structural and optical equilibrium properties of the samples. In the following, we present a detailed analysis of the absorption-saturation data and their modeling based on the simulation approach developed in Task 3.3. Moreover, using the same FEL pumping scheme as for absorption-saturation experiments, we directly measured THz photon emission from ISBTs of a TB MQW sample. We will show that the ISBT PL efficiency observed is in reasonable agreement with that expected by the model.

The second set of experiments was carried out at FELBE in May 2019 and focused on the measurement by time-resolved single-color pump-probe spectroscopy of non-radiative lifetimes (i) in coupled MQW systems with TB and NTB designs and (ii) in single MQWs of different well widths under 1- \rightarrow 2 optical pumping.

THz absorption-saturation in Ge/SiGe MQWs

In an absorption saturation experiment, electrons are excited from level 1 to level 3 with an intense optical source resonant with E_{13} and the output intensity (I_2) is measured as a function of the variable incoming intensity (I_1) [Fig. 7(a)].

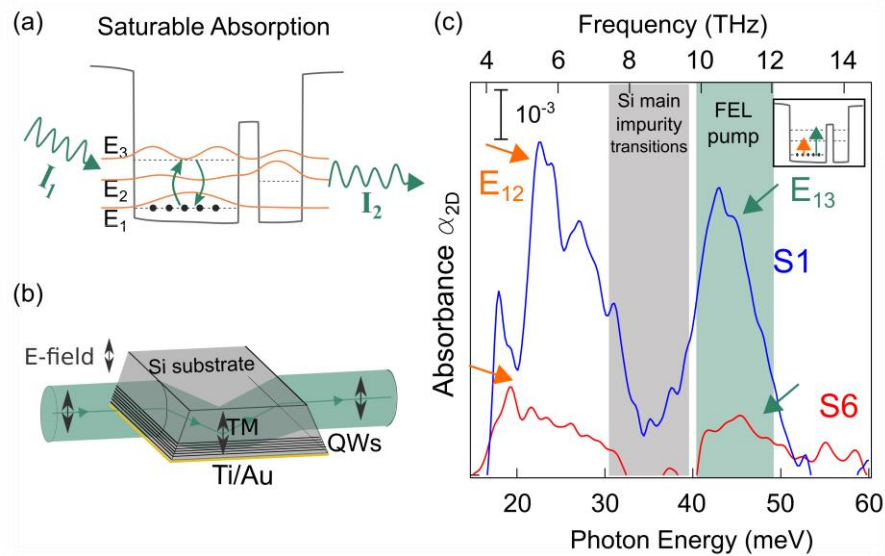


Fig. 7. (a) A sketch of the saturable absorption process: electrons are excited with an intense optical source, at the E_{13} , from level 1 to level 3 and the output signal (I_2) is measured as a function of the variable incoming signal (I_1). **(b)** A sketch of a single-pass waveguide allowing optical coupling to the QWs region. The TM-polarized electric field direction is indicated with a double-headed arrow. **(c)** The absorbance spectra of the two investigated samples S1 and S6, featuring two clear peaks corresponding to the $1 \rightarrow 2$ and $1 \rightarrow 3$ ISBTs, as sketched in the inset. Absorbance of sample S6 is less intense, as expected from less doping. The region of the pump photon energies E_{13} used for the experiment is reported as a green-shaded area, which is just outside the energy range at which the most relevant transitions of the Silicon wafer impurities are present (grey-shaded area).

The samples investigated are the asymmetric-coupled TB MQWs S1-2216 and S6-2219 made of 20 identical modules featuring a wide Ge well of 12(11.5) nm and a narrow Ge well of 5 nm separated by a $\text{Si}_{0.15}\text{Ge}_{0.85}$ tunneling barrier. The modules are separated by a 21 nm-thick $\text{Si}_{0.2}\text{Ge}_{0.8}$ spacer. S1 is heavily n-doped in the wide quantum well to $7 \times 10^{11} \text{ cm}^{-2}$ while S6 is n-doped to $1 \times 10^{11} \text{ cm}^{-2}$. Optical coupling to the MQW region is obtained by shaping the samples into the prism single-pass waveguide geometry sketched in Fig. 7(b). The heterostructure design targeted a comparable $1 \rightarrow 2$ and $1 \rightarrow 3$ oscillator strengths, obtained through strong hybridization of levels 2 and 3. Beyond increasing the optical pumping efficiency, this condition also enabled us to measure clear intersubband absorption signatures of both $1 \rightarrow 2$ and $1 \rightarrow 3$ ISBTs by absorption spectroscopy at equilibrium performed by FTIR at 10 K. This is evident in the equilibrium 2D absorption coefficients reported in Fig. 7(c) which show two peaks centered at the photon energies E_{12} and E_{13} in both samples S1 and S6, with intensity ratio between S1 and S6 approximately matching the doping level ratio of 6. If compared between themselves in both samples, the two peaks have similar intensity, as targeted in the design, indicating strong hybridization between the excited states of the two coupled wells. As discussed in Section 2, the energies of the absorption peaks match well with the depolarized ISBT energies predicted by the Schrödinger-Poisson solver (See Fig. 1). The precise determination of the pump transition energy E_{13} from the absorption spectra has allowed us to precisely tune the optical pump photon energy at the $1 \rightarrow 3$ ISBT maximum at 10.5 THz, or to

detune it in a controlled way if required for example to avoid the energy range at which the most relevant transitions of the Silicon wafer impurities are present [grey-shaded area in Fig. 7(c)].

Optical pumping of the $1 \rightarrow 3$ ISBT was experimentally achieved with quasi-monochromatic THz pulses from the FEL tuned at pump photon energies of 41.9 - 48.1 meV around E_{13} (338 - 387 cm^{-1} , 10.2 - 11.7 THz, or 25.8 - 29.6 μm) [19]. The pulse duration was $\Delta t_p \sim 10$ ps with a Gaussian envelope, resulting in approximately 100 radiation cycles per pulse. The maximum peak power of $P_{in,max} = 15$ kW, calculated from a measured continuous-wave (CW) FEL power of 2.0 W and a duty cycle of 1.3×10^{-4} , results in a maximum peak pump intensity in vacuum $I_{p,max,vac} = P_{in,max}/\pi r^2 = 1.9 \times 10^6$ W/ cm^2 , where $r \sim 0.5$ mm is the radius of the focal spot determined inserting a THz camera at the sample position. The pump intensity in the ACQW region is much lower than this vacuum value mainly because a copper screen with rectangular slit aperture of 0.3×5.0 mm^2 , much smaller than the waveguide section of 0.5×8.0 mm^2 , was mounted before the sample in order to avoid any pump radiation to pass through the cryostat without passing through the waveguide. The combination of diffraction losses, electromagnetic mode mismatch at the waveguide input-facet and reflections at the cryostat windows leads to an estimated optical coupling loss factor $l \sim 6 \times 10^{-3}$. Thus, The actual pump intensity in the MQW region is $I_{p,max} = l P_{in,max}/\pi r^2 \sim 11$ kW/ cm^2 corresponding to $F_{p,max} \cong \Delta t_p I_{p,max} \sim 0.11$ $\mu\text{J}/\text{cm}^2$. The saturation of absorption due to the pump action in the three-level ACQW system was measured by increasing the FEL pump beam intensity from almost zero to maximum available power using a set of metal mesh attenuators. The samples were mounted in the sample holder so as to have the FEL radiation in TM-polarization inside the slab waveguide. Simultaneously, the incident radiation intensity I_1 (or in terms of power P_{in}) and the transmitted intensity I_2 (or power P_T) were measured with calibrated pyroelectric detectors [see Fig. 8(d) for a scheme of the optical setup]. Similarly, to the FTIR experiment, the samples were kept at cryogenic temperatures ($T = 6$ K) in the optical He-flow cryostat.

In Fig. 8(a-b) the $T(F_p)$ plots show the transmittance $T = I_2/I_1 = P_T/P_{in}$ as a function of the fluence $F_p = \ell \Delta t_p P_{in} / \pi r^2$ for S1 and S6, at the three pump photon energies explored. The zero-fluence transmittance $T_0 = T(F_p \rightarrow 0)$ is calibrated with a Lorentz oscillator model of the transmittance based on FTIR data for each sample, temperature and pump photon energy [Fig. 8(c)].

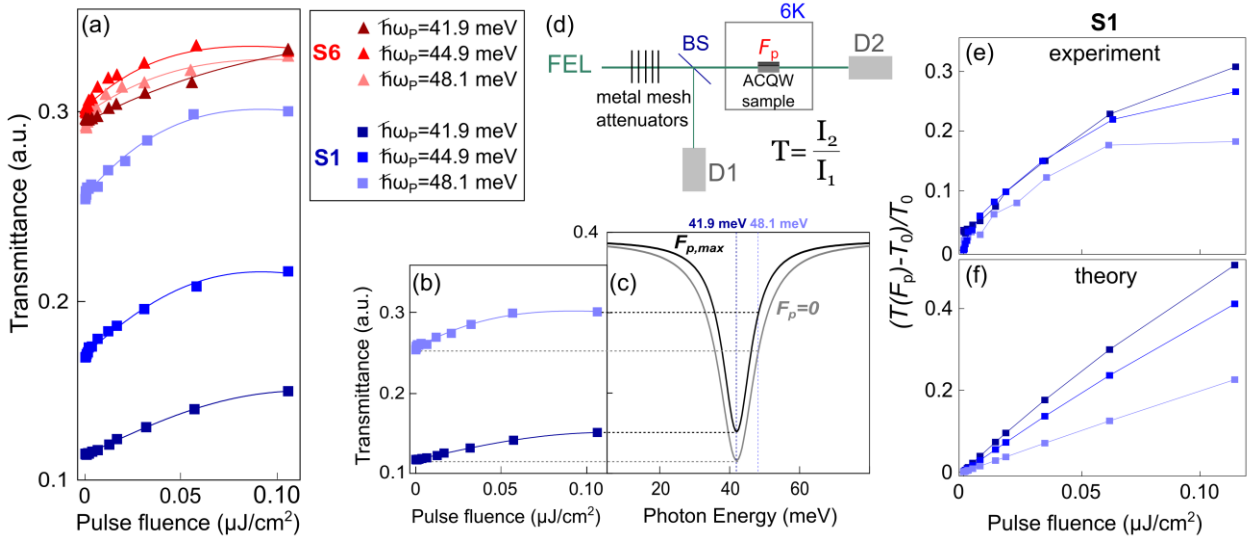


Fig. 8. (a) The transmittance measured as a function of the pump fluence for both the investigated samples at the three photon energies, as reported in the legend. **(b)** Same quantity as panel (a) for S1 at $\hbar\omega_p = 41.9$ meV (dark blue curve) and $\hbar\omega_p = 48.1$ meV (light blue curve) to show how the transmission spectrum at 6 K, sketched in panel c, changes at $F_p \rightarrow 0$ and $F_{p,max}$. Panels (b) and (c) have the same vertical scale and the dotted lines are a guide to connect the transmittance at $F_p \rightarrow 0$ and $F_{p,max}$ for these two photon energies. **(d)** A sketch of the setup used for the experiment: the fluence level is set by metal mesh attenuators placed before the beam splitter (BS). The experimental and the theoretical relative transmittance variations for sample S1 at 6 K are reported in panel (e) and (f). For the experimental determination, the value T_0 is the FTIR transmittance at zero fluence, which has been subtracted to the data in panel (b). Numerical data in panel (f) have been obtained as discussed in the text.

A nonlinear increase of $T(F_p)$ is clearly seen in Fig. 8(a) at all the investigated pump photon energies for both samples. In particular, the lightly doped sample S6 demonstrates a transmission increase of 10% at $F_{p,max}$ at all $\hbar\omega_p$, whilst the heavily doped sample reaches an increase of transmission above 25% for resonant pumping at $\hbar\omega_p = 41.9$ meV. This is consistent with the effectiveness of heavy doping in increasing the amount of saturable ISBT losses with respect to non-saturable optical transmission losses. We will now show how the overall scenario is quantitatively confirmed by the simulated non-equilibrium population dynamics.

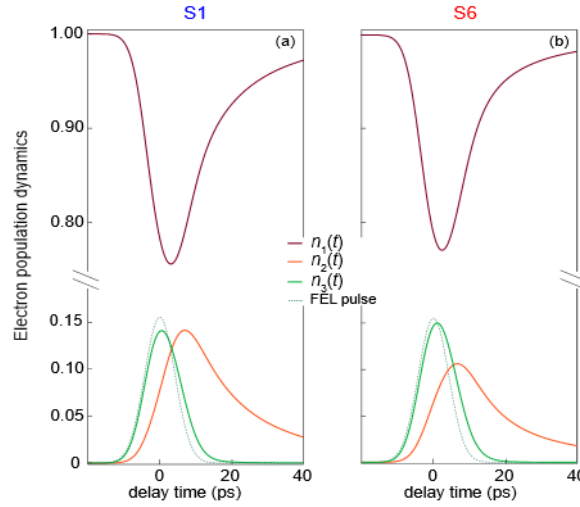


Fig. 9. Electron population dynamics $n_i=N_i/N_{\text{tot}}$ for sample S1 (a) and S6 (b), simulated at a lattice temperature set to a lattice temperature of 6 K. The time envelope of the pump pulse used in the simulations is also reported as a dotted line.

In Fig. 9, we report the numerical simulations of the population dynamics for the two investigated samples under optical pumping using the same experimental value of $I_{p,\text{max}} = 11 \text{ kW/cm}^2$ as pump intensity. Population dynamics of the upper state $n_3(t)=N_3(t)/N_{\text{tot}}$ closely tracks the time profile of the pump pulse (dotted lines in Fig. 9). A peak value $n_{3,\text{max}}$ ranging between 0.14 and 0.15 is obtained in all our samples. Fitting the calculated temporal evolution of the subband populations $n_2(t)$ and $n_3(t)$ with an exponential decay function starting after the excitation pulse peak, we obtain the lower subband lifetime $\tau_{\text{relax},2} \sim 17 \text{ ps}$ for S1 and 15 ps for S6 and the upper subband lifetime $\tau_{\text{relax},3} \sim 3 \text{ ps}$ for S1 and 6 ps for S6.

We now discuss how from the dynamic model we can estimate the transmission variation $= (T(F_p) - T_0)/T_0$, to be compared to experimental counterpart. We first evaluate, at each fluence, the absorption coefficient $\alpha_{13}(F_p) = \alpha_{13}(F_p) = C(f_{13}/m^* \sqrt{\epsilon_r})(N_1 - N_3)$, where $\epsilon_r = 16.0$ is the dielectric constant of Ge, $C = (\pi e^2)/(2\epsilon_0 c \Delta\omega)$ is a dimensional constant and $\Delta\omega \sim 10^{13} \text{ s}^{-1}$ is the ISBT linewidth. Clearly the absorption coefficient α_{13} varies over delay times, according to the time evolution of N_1 and N_3 populations. Here, $\alpha_{13}(F_p)$ has been determined from the model as the value corresponding to the minimum population difference $N_1 - N_3$ achieved for a given pulse fluence level, typically reached at times close to $t = 0$. The fluence-dependent transmittance is calculated as $T(F_p) = \exp(-\alpha_{13}(F_p)L)$ where L is the equivalent optical path length in the QWs, which depends on the number of repetitions of the ACQW structure (here equal to 20), on the internal reflection angle $\theta_{\text{in}} = 75^\circ$, and on the physical waveguide length [20]. From $T(F_p)$, we evaluate the relative transmittance change $\Delta T(F_p)/T_0 = (T(F_p) - T_0)/T_0$, with respect to the value T_0 [Fig. 8(e)], which is the transmittance at zero fluence estimated by FTIR. We find fair agreement with the same quantity determined experimentally for all the pump photon energies employed [compare Figs. 8(e) and 8(f)]. In a saturable absorber [19-22], a very important parameter is the saturation fluence $F_{p,\text{sat}}$, defined as the optical pump intensity level at which the transmittance at the pump photon energy is changed

by a factor of $1/e$ with respect to its maximum achievable increase, often corresponding to that at which the absorption decreases below one half of its equilibrium value, due to depopulation of level 1 and simultaneous population of level 3. From the $\Delta T(F_p)$ behavior, we then obtain $F_{p,sat,num}$ as the fluence at which the transmittance change reaches a factor $1/e$ of its saturated value. An example is reported in Fig. 10 for one of photon energies employed.

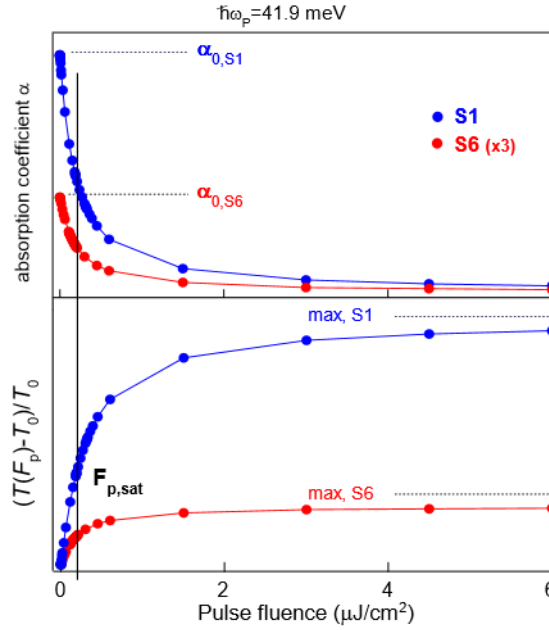


Fig. 10: The simulated absorption coefficient (upper panel) and the relative transmittance variation (lower panel) as a function of the pulse fluence for sample S1 (blue curves) and S6 (red curves). For comparison, the lower signal for the less-doped S6 has been multiplied by 3. The lattice temperature has been set to 6 K.

Following the described procedure, we obtain a numerical estimate of $F_{p,sat,num} = 0.17 \mu\text{J}/\text{cm}^2$ which, within the uncertainties due to numerical sampling of the fluence (See Fig. 10), is found to be sample-independent. The model indicates that that a fraction of the order of 15% of the electrons in the ground state 1 is excited to the level 3 under optical pumping with the maximum available FEL pulse fluence $F_{p,max} = 1.1 \times 10^{-7} \text{ J}/\text{cm}^2 \sim 0.6 F_{p,sat,num}$.

THz intersubband emission

We have then used the same maximum fluence $F_{p,max} = 0.11 \mu\text{J}/\text{cm}^2$ obtained in the absorption saturation experiment for measuring the radiative THz PL emission of ISBTs. To this aim, we replaced the second pyroelectric detector (D2) in Fig. 8(d) with a Michelson interferometer and a liquid-He bolometer [Fig. 11(a)]. The collection mirror after the cryostat was a 50-mm diameter parabolic reflector with a focal length of 100 mm, therefore emission angles up to $\pm 14^\circ$ outside the waveguide were collected, which corresponds to $\pm 4^\circ$ inside the waveguide according to Snell's law [Fig. 11(b)]. For this measurement, we selected the TB MQW sample 2217-S2 (characterized by FTIR in Ref. [12], see also Deliverable 3.1) which features $w_L = 13 \text{ nm}$ and the same other structural parameters as S1, S6, being, however, heavily doped with $n_{2D} = 9 \times 10^{11} \text{ cm}^{-2}$ for

maximizing the output emission power. The FEL pump photon energy was 44.4 meV with a detuning of +4.8 meV with respect to $E_{13}^{FTIR} = 39.6$ meV ([12], see Deliverable 3.1). The detuning was meant to limit pump absorption in the silicon wafer associated to the impurity transition line at 39 meV. The effect of this small detuning on the pump efficiency is not critical, as observed in the analysis of Fig. 8. A long-wavelength pass filter [2 mm thick z-cut quartz plate, whose polarization-dependent transmittance is shown in Fig. 11(c)] was used in front of the bolometer to screen it from the direct FEL pump beam. The attenuation of the quartz plate at the pump photon energy of 44 - 45 meV is estimated in the range of 10^{-8} , making the residual FEL power smaller than the blackbody background. A wire-grid polarizer was inserted before the bolometer to switch between TM- or TE-polarized emission, while the pump was always kept in TM-polarization.

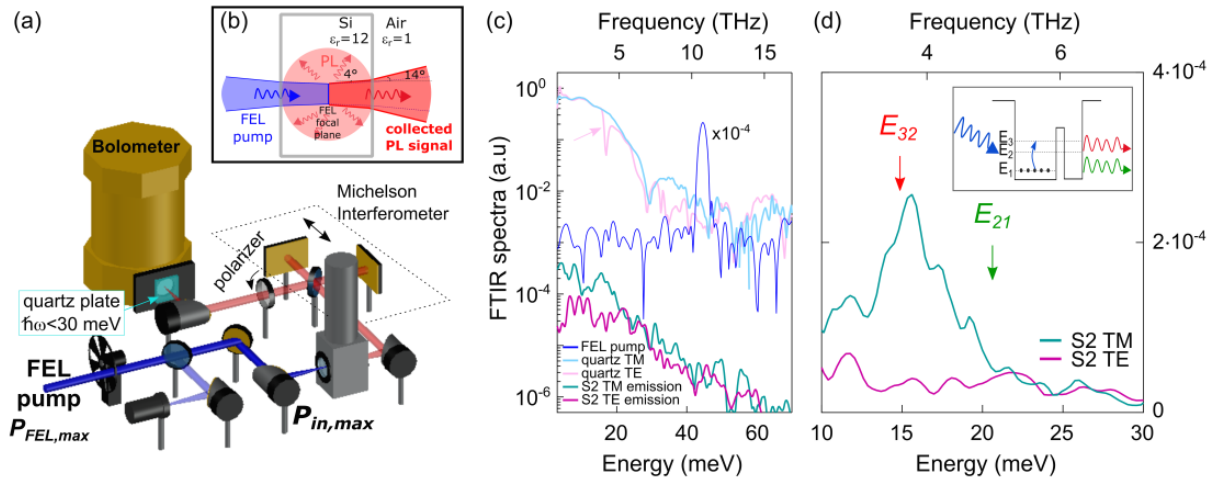


Fig.11. (a) A sketch of the experimental setup used for the THz-PL measurements. **(b)** Details of the collection angle of the PL emission, in a top view, are also reported: note that the PL emission is isotropic in the in-plane direction (red shaded circular region), but the emission is collected with a $f/2$ parabolic mirror hence with a maximum marginal angle $\varphi = \pm 14^\circ$ (corresponding to $\varphi_{in} = \pm 4^\circ$ inside the sample, according to Snell's law.) **(c)** The Fourier-Transform emission spectra of sample S2 corresponding to the TM- and TE-polarized emitted signals (green and purple curves, respectively), plotted together with the polarization-dependent FTIR transmission spectra of the quartz plate (light blue -TM- and pink -TE- curves) and the FEL pump signal (blue curve- attenuated to 10^{-4}), all on a log scale. The pink arrow indicates the z-cut quartz phonon absorption present only in TE-polarization. **(d)** A zoomed image of the TM and TE signals on a linear scale. The color arrows are located at the position of the theoretical transition energy. The PL process is sketched in the inset of the panel (d). Cryostat base temperature was 6 K in all experiments.

The TM and TE emission spectra of sample S2 are shown in Fig. 11(c) on a logarithmic scale and zoomed in Fig. 11(d) on a linear scale. An emission peak centered around 16 meV is clearly observed in the TM emission spectrum (green curve). This value is in good agreement with the estimated $3 \rightarrow 2$ ISBT energy ($E_{32} = 14.6$ meV). However, since the $2 \rightarrow 1$ ISBT energy $E_{21} = 20.4$ meV is close to E_{32} , also photon emission from this transition may contribute to the observed PL emission peak. Indeed, our numerical simulations indicate that the time-integrated number of photons associated to the $2 \rightarrow 1$ transition should be comparable to that due to the $3 \rightarrow 2$ transition.

The emitted ISBT-PL peak power has been estimated from the comparison of the TM emission spectrum [green curve in Fig. 11(c)] with the (attenuated) pump line measured with the same detector [blue curve in Fig. 11(c)]. The energy-integrated ISBT-PL emission peak power is found in the range of 10 to 100 μ W, where the uncertainty is due to non-linearity of the detector response. Assuming isotropic in-plane emission of the vertical ISB dipole [red shaded circular area Fig. 11(b)] [21], we obtain a factor $4^\circ/180^\circ = 0.022$ for the collected emission and then a calculated peak power emitted in all directions of 0.45 to 4.5 mW, corresponding to a ISBT-PL efficiency of the order of 10^{-7} . This value is in a good agreement with a rough estimation of the quantum efficiency $\eta_{\text{Ge}} \sim \tau_{\text{relax},3}/\tau_{\text{rad},32}$ based on our model. As mentioned before, the upper subband lifetime $\tau_{\text{relax},3}$ predicted by our dynamic model for TB samples with the typical parameters employed here is in the order of 3 to 6 ps (Fig. 9) while the radiative lifetimes [27] is estimated to be $\tau_{\text{rad},32} \sim 20 \mu\text{s}$.

Non-radiative lifetimes measurement by pump-probe spectroscopy

We now discuss the calibration of the model based on the measurements of time-resolved single-color pump-probe spectroscopy of non-radiative lifetimes (i) in coupled MQW systems with TB and NTB designs and (ii) in single MQWs of different well widths under 1- \rightarrow 2 optical pumping. The calibration essentially concerns the relevant values for the effective interface roughness parameters controlling the IFR scattering and the effective deformation potentials for the electron-phonon interaction Ξ_{OP} for the intervalley phonon at $\hbar\omega_{\text{eff}} = 27.56$ meV and the intravalley phonon at $\hbar\omega_{\text{eff}} = 37.07$ meV [11]. As mentioned before and detailed in D1.5, an IFR RMS amplitude $\Delta = 0.18$ nm and a correlation length $\Lambda = 6.9$ nm have been obtained from the APT experiments. On the other hand, the general model for the IFR scattering in diffuse interfaces we have developed (see again D1.5) revealed that, when the interface roughness is vertically correlated along the growth axis on a smaller length than the interfacial width as measured in our samples by the APT experiment, the interface does not behave as a single scattering center, but rather acts as several scattering layers which are only partially correlated. This ultimately translates into a significant reduction of the effectiveness of the IFR potential which can be accounted for with a reduced effective value of IFR RMS amplitude $\Delta_{\text{eff}} = 0.11$ nm.

The values for optical phonon coupling constants in Ge had been taken from Monte Carlo calculations calibrated with drift velocity and diffusivity experiments [11]. There are some experimental reports that suggest, however, weaker electron phonon interactions than that predicted from the calculated deformation potentials [7,22]. Since the intersubband coupling of 2D electrons to phonons strongly depends on the ISBT energy with respect to phonon energy thresholds, a detailed analysis of the non-radiative lifetimes as a function of the ISBT energies is required for a proper calibration.

We first see what to expect from the simulation standpoint and then compare to experimental results. In Fig. 12, we show the calculated evolution of the first-excited state L_2 population after resonant E_{12} optical pumping for single MQWs of different Ge well thickness (i.e. E_{12} ISBT energy). The spacers between the wells are, as usual, $\text{Si}_{0.20}\text{Ge}_{0.80}$. We fixed the pump intensity so that 1% of the electrons are excited into level 2. The total n_{2D} electron density is $1 \times 10^{11} \text{ cm}^{-2}$. We run the

simulations with all the elastic and inelastic channels on and by turning off, one-by-one, the elastic channels (IFR+Coulomb) or each of the inter- and intra-valley phonon scatterings. By inspecting Fig. 12, the following observations can be made:

- Below the intervalley phonon threshold, the relevant relaxation mechanism is the elastic (IFR+Coulomb) one. Being below both of phonon thresholds, the lifetime increases significantly reaching values of several hundreds of ps when the elastic mechanisms are turned off. This clearly shows how important is the inclusion of the elastic relaxation mechanisms for meaningful lifetime simulations, also in the case of single MQWs.
- Above the intervalley phonon threshold, the lifetime increases significantly only when the intervalley mechanism is turned off. This shows that above its threshold, the intervalley phonon scattering is dominant, while the elastic contribution to the relaxation is only marginal for single MQWs.
- Going above the intravalley phonon threshold, one observes an increase in the lifetime only when the intervalley phonon is off. This means that the relaxation pathway through the intervalley is still acting and relevant at high energy level separations.

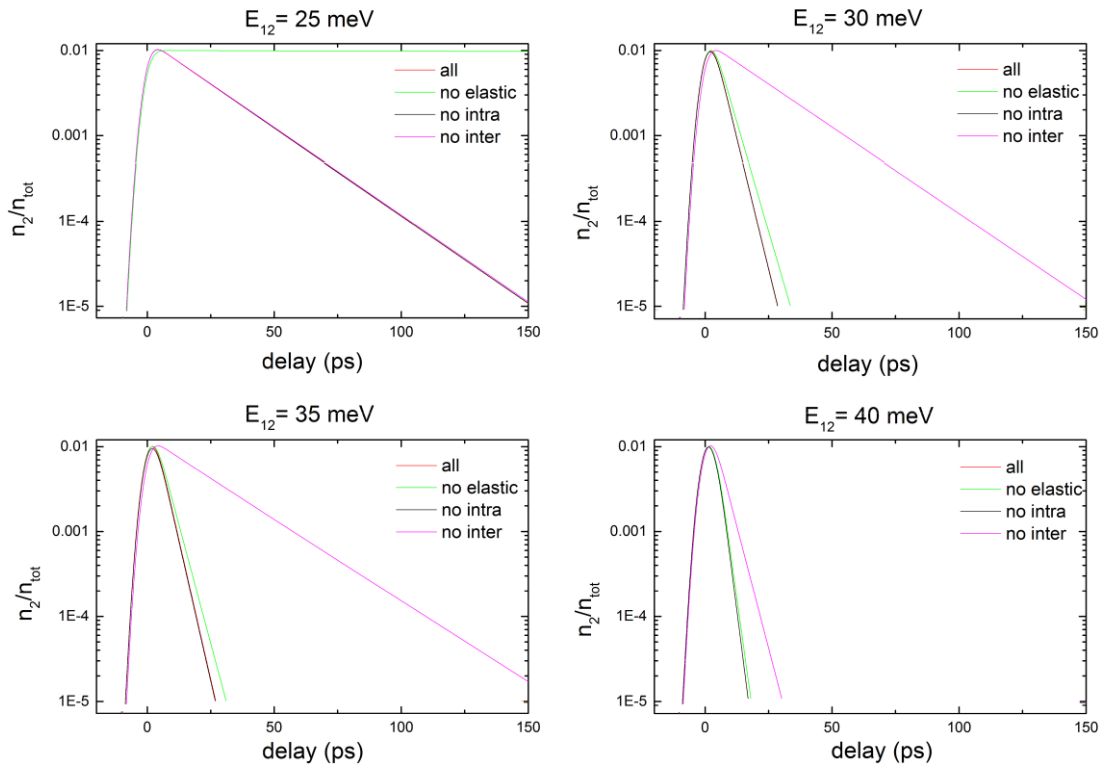


Fig. 12. First-excited state L_2 population as a function of the probe delay after resonant E_{12} optical pumping predicted by the model for single MQWs of different Ge well thickness (i.e. E_{12} ISBT energy). We set the pump intensity so that 1% of the electrons are excited into level 2. The total n_{2D} electron density is $1 \times 10^{11} \text{ cm}^{-2}$. We run the simulations with all the elastic and inelastic channels on and by turning off, one-by-one, the elastic channels (IFR+Coulomb) or each of the inter- and intra-valley phonon scatterings.

It is now interesting to draw a comparison between single and TB-coupled MQWs. Figure 13 shows the upper excited state lifetime τ_{31} calculated for a TB configuration as a function of the E_{13}

energy for resonant 1-3 optical pumping. The plot is obtained by varying w_L and fixing $b_t = 2.3$ nm and the width of the thin Ge well to 5 nm. The doping density is $n_{2D} = 5 \times 10^{11} \text{ cm}^{-2}$. The Ge content is 87% for the tunnel barrier and 80% for the SiGe spacers.

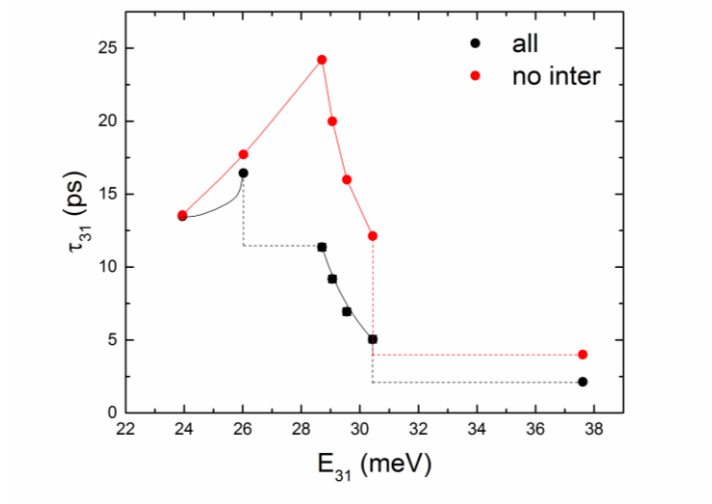


Fig. 13. Relaxation time τ_{31} calculated for a TB configuration as a function of the E_{13} energy for resonant 1-3 optical pumping. The plot is obtained by varying w_L and fixing $b_t = 2.3$ nm and the width of the thin Ge well to 5 nm. The doping density is $n_{2D} = 5 \times 10^{11} \text{ cm}^{-2}$. The tunneling barrier has a Ge content of 87%.

From inspecting Fig. 13, we notice the following points:

- Below the intervalley threshold, the lifetime increases with the energy since the relaxation is dominated by the elastic processes which are faster at small energy separations, since in this case the exchanged momentum in an elastic process is smaller. As expected, turning off the intervalley phonon scattering has limited impact.
- Across the intervalley threshold around 27 meV, the lifetime drops when the intervalley phonon mechanism is on, whereas it still goes up due to the elastic pathway when the intervalley is switched off.
- Above 29 meV, the lifetime decreases for both scenarios: the decrease is faster when the intervalley is off, since the approaching of the intravalley threshold at 37 meV becomes the dominant process.
- When the intervalley is kept on, both the phonons contribute to the decrease in the lifetime at large ISBT energies. As in the case of single MQWs, the intravalley threshold is particularly evident when the intervalley is off. This indicates that intervalley scattering is still acting, also at high energies.

From what we learnt from simulations, it is clear that, for calibrating the IFR scattering parameter, one has to design structures where the ISBT of interest occurs below the intervalley threshold (< 27 meV). The relative weight of IFR among the other elastic channels can be tuned by changing the symmetry of the structure and therefore the wavefunction penetration across the interfaces, comparing for example a single-well design to a NTB and TB asymmetric configurations. Experimentally, we therefore investigated by single-color pump

probe spectroscopy the three structures sketched in Fig. 14, pumping the E_{12} ISBT which occurs between 19 and 24 meV for these structures, as shown by the FTIR dichroic transmission spectra reported in the figure. The intersubband non-radiative lifetimes were measured in a degenerate pump-probe scheme with the FEL emitting a continuous train of pulses (duration from 4.8 ps for $h\nu_{\text{FEL}}$ 28.8 meV, with separation of 77 ns). The pump power was reduced by a set of attenuators to 40 mW (power density at focus around 6 kW/cm²). Apart from dynamic depolarization shift effects arising when the pump is several meV redshifted from the ISBT absorption energy (not the case here) [4], the temporal evolutions of the carrier population as a function of pump-probe delay follows that of the relative differential transmission signal $\Delta T(t)/T(t=-\infty)$ [7]. Despite a level of noise which was unfortunately particularly high during our experiment due to some beam instability, the experimental differential transmission (red dots) shows a markedly different dynamics for the three samples following the behavior expected for the increasing impact of IFR scattering. A single-exponential fit to the data gives a non-radiative lifetime on the order of 34 ps for the single MQW 2263 (leftmost panel in Fig. 14) which is reduced to 23 ps for the 2264 NTB configuration with a Si_{0.03}Ge_{0.97} step (middle panel in Fig. 14). The relaxation of the TB sample 2216-S1 (rightmost panel in Fig. 14) could not be measuring appearing faster than the time resolution of the setup (about 10 ps).

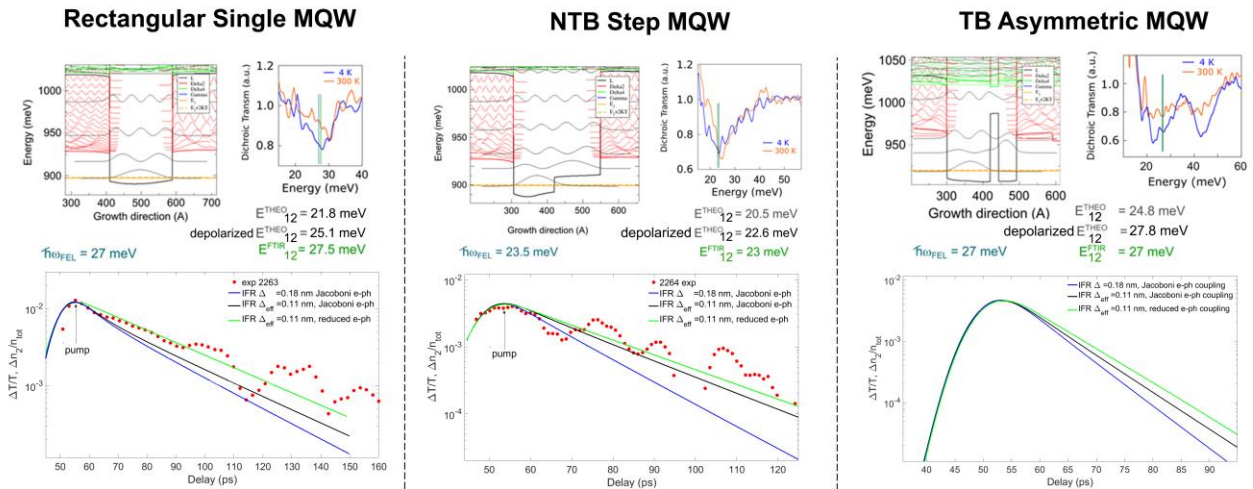


Fig. 14. Top panels: Calculated electron energies, squared wave functions and measured FTIR dichroic transmission spectra $T_{\text{TM}}/T_{\text{TE}}$ for symmetric and asymmetric MQW samples. Bottom panels: Under 1->2 optical pumping the corresponding experimental differential transmission (red dots) and simulated level 2 population as a function of the probe delay are reported. The simulated curves are shown for different values of RMS IFR amplitude and optical phonon deformation potentials.

The dynamics of the relaxation has been simulated in Fig. 14 by tuning both the deformation potentials for electron coupling to inter- and intra-valley phonons in Ge as well as with two different values of the IFR RMS amplitude $\Delta = 0.18$ nm and $\Delta_{\text{eff}} = 0.11$ nm. As mentioned before, the former is the value measured by APT and the latter is the effective value obtained from the theoretical analysis discussed in D1.5, when taking into account the presence of a finite vertical

correlation among interfaces. As for the deformation potentials, we remind from Table 1 that the tabulated value by Jacoboni et al. [11] are $\Xi_{OP}^{inter} = 3.0 \times 10^8$ eV/cm and $\Xi_{OP}^{intra} = 5.5 \times 10^8$ eV/cm, respectively. We reduced the strength of the electron-phonon coupling by using $\Xi_{OP,eff}^{inter} = 0.25 \times 10^8$ eV/cm and $\Xi_{OP,eff}^{intra} = 2.1 \times 10^8$ eV/cm. This choice has been done on the basis of pump-probe data acquired on isolated MQWs samples having different thickness and E_{21} intersubband energy separation below and above the threshold for inter and intra-valley phonons, reported in Fig. 15 and discussed in the following. Furthermore, all the simulations reported in Figs. 14 and 15 have been carried out with the carrier density n_{2D} obtained from FTIR experiments on each sample and using the pump intensity required for a peak population imbalance corresponding to the peak differential transmission measured.

In order to calibrate in our model IFR scattering parameters we first focus on the step MQWs and the TB coupled ACQWs in Fig. 14. We notice that the dynamics in these structures is strongly sensitive to the IFR parameter and depends only slightly on the electron-phonon coupling constants, confirming the dominant role of this elastic relaxation pathway below the intervalley phonon threshold. By using the Jacoboni et al. deformation potentials, we obtain, for the TB case, a τ_{21} lifetime of 6.3 ps and 7.3 ps for $\Delta = 0.18$ nm and $\Delta_{eff} = 0.11$ nm respectively. Whereas by reducing the electron-phonon coupling constants with Δ_{eff} for IFR, the lifetime is increased to 8.3 ps. All the predicted lifetimes are below the time resolution of the experimental setup, explaining why we could not detect the ISBT dynamics in the experiment. More relevant for the calibration purpose is the NTB case which shows slower and experimentally detectable dynamics. By visually inspecting Fig. 14, it is clear that, for the NTB sample, the $\Delta = 0.18$ nm IFR amplitude value results in a relaxation dynamics much faster than what observed experimentally ($\tau_{21} = 12$ ps instead of 23 ps). On the contrary, it is clear that the $\Delta_{eff} = 0.11$ nm value gives a lifetime in close agreement with the experiment. Thus, below the lowest phonon threshold, one needs to use an effective IFR RMS amplitude of about 0.11 nm in order to catch the relaxation dynamics. We recall that this effective lower value of the IFR RMS amplitude can be attributed to reduced effectiveness of the IFR due to the presence of a finite axial correlation within the interfaces observed in APT data (See D1.5).

We now focus on a set of single-MQWs which are designed to obtain a E_{12} level spacing ranging from 12 to 47 meV, by varying the Ge well width in the 24-10 nm range. By optically pumping the E_{12} ISBT, this allows us to cross both the inter- and intravalley phonon thresholds and get a more accurate calibration of the electron-phonon coupling constants. The results of the single-color pump-probe experiment and the corresponding simulations are shown in Fig. 15. The simulations are performed with the $\Delta_{eff} = 0.11$ nm for IFR and with both the Jacoboni (black curves) and the reduced (green curves) electron-phonon constants for inter- and intra-valley OP scatterings. We first focus on the MQW samples where the ISBT is below the intervalley phonon energy. For the lowest ISBT energy (sample 1745), the black and green curves coincide, indicating that electron-phonon scattering are not the dominant relaxation process. At such low level spacing $E_{12} = 12$ meV, despite the high pump intensity used ($\Delta n_2/n_{tot} \sim 30\%$) produces a high electronic temperature T_e , the maximum kinetic energy of electrons within the tail of the Fermi distribution in L_2 is not

enough to enable the emission of intervalley OPs and, thus, the elastic processes are the most effective scattering events. The agreement of experimental data and the theoretical curve confirms the need to use $\Delta_{\text{eff}} = 0.11$ nm to model the IFR scattering rate. For a slightly larger $E_{12} = 19$ meV closer but still below the intervalley phonon energy (sample 2263), we start detecting a difference between the Jacoboni and the reduced deformation potentials, due to the finite energy broadening of L_2 electron distribution. However, both the simulated behaviors may still describe appropriately the experimental data within the experimental uncertainty. Note that the pumping level for 2263 is relatively low, giving a peak $\Delta n_2/n_{\text{tot}} \sim 3\%$, and, thus, most of electrons in L_2 have kinetic energies below the intervalley phonon threshold.

Above the intervalley-phonon threshold (middle and bottom panels in Fig. 15), it is clear that the Jacoboni deformation potentials result in a relaxation dynamic being much faster than that observed in the experiment. In between the inter- and intra-valley thresholds (middle panel in Fig. 15), the stronger effect is that of the intervalley coupling constant which we varied from the Jacoboni value until a reasonable fitting of all the data curves is obtained. The best-matching value is indeed observed for $\Xi_{OP,eff}^{\text{inter}} = 0.25 \times 10^8$ eV/cm, i.e. more than one order of magnitude smaller with respect to the Jacoboni value. As previously mentioned, this finding supports the claim by Sun *et al.* [22] that the intervalley processes should be suppressed in this kind of multilayer structures. Note that for these simulations, we used $\Xi_{OP,eff}^{\text{intra}} = 2.1 \times 10^8$ eV/cm but very similar behaviors are found even with the Jacoboni intra-valley value $\Xi_{OP}^{\text{intra}} = 5.5 \times 10^8$ eV/cm, showing that, below the intravalley threshold, the effect of reducing the intravalley coupling constant is almost negligible.

We now focus on the sample 2261 (bottom panel in Fig. 15) for which the ISBT is well above the intra-valley phonon energy, ensuring the activation of the intra-valley OP scattering even at the low pumping powers employed. We notice that the relaxation dynamics of 2261 cannot be reproduced by changing only the intervalley deformation potential and keeping the Jacoboni value for the intravalley scattering (dashed green curve): to match the experiment, one has to reduce as well the intravalley deformation potential to the value $\Xi_{OP,eff}^{\text{intra}} = 2.1 \times 10^8$ eV/cm (green full curve). Notice that, as shown in Fig. 15 (lower panel), the experimental decay measured in this sample at different pumping powers and lattice temperature is well reproduced using the same value of the deformation potential coefficients.

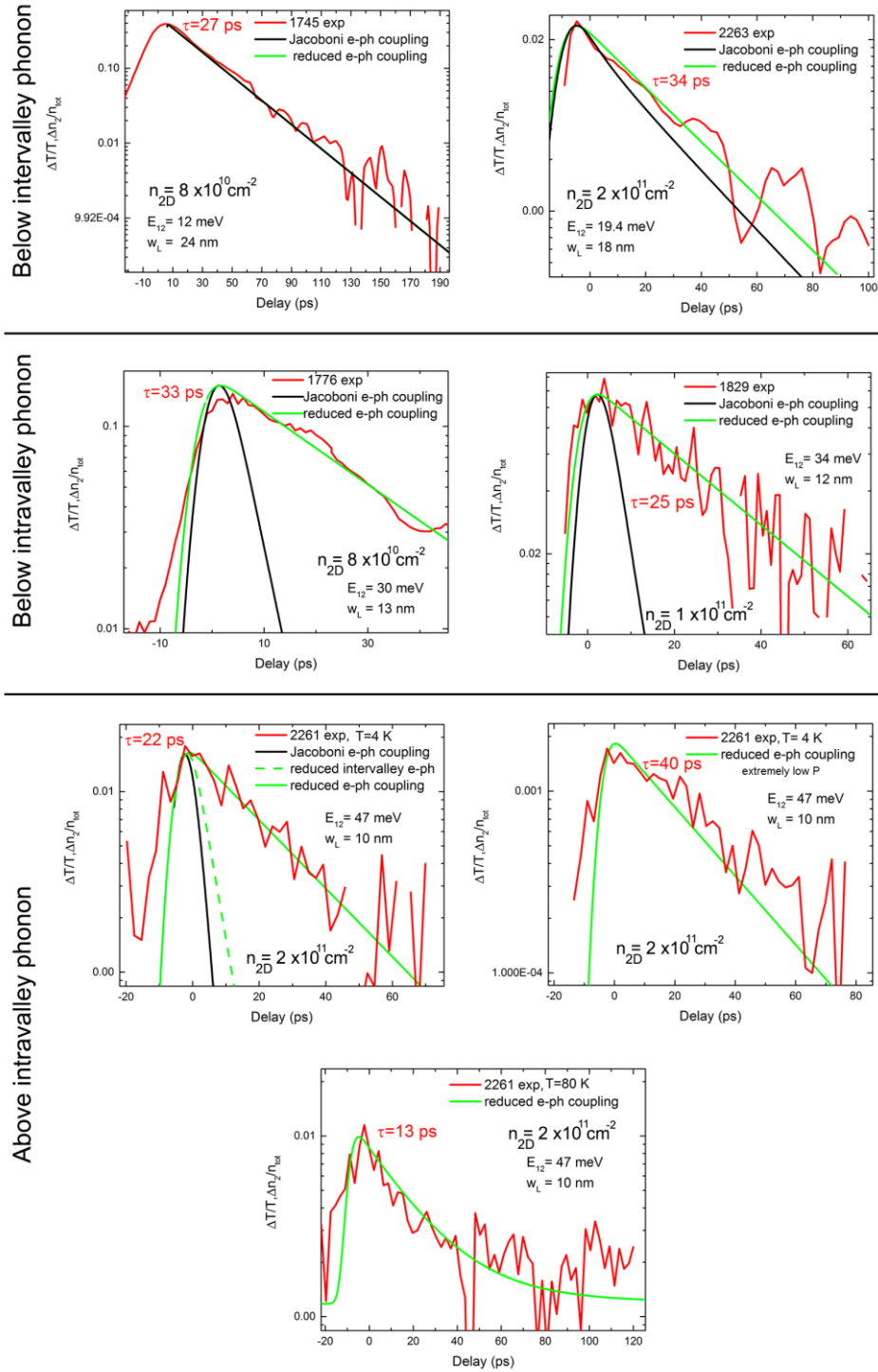


Fig. 15. Single MQW structures under 1->2 optical pumping as a function of the Ge well width (i.e. E_{12} subband energy separation): experimental differential transmission (red curves) and simulated L_2 populations as a function of the probe delay are reported. All the simulations are carried out with IFR RMS amplitude $\Delta_{\text{eff}} = 0.11$ nm. The black curves are obtained with the Jacoboni deformation potentials, the full green curves with the reduced effective deformation potentials $\Xi_{OP,eff}^{int,ra}$ and $\Xi_{OP,eff}^{inter}$ reported in the text, while the dashed green curve with $\Xi_{OP,eff}^{inter}$ for the intervalley scattering and the Jacoboni coupling for the intravalley scattering.

In summary, the fact that even above the intravalley threshold the decay of the differential transmission signal observed experimentally still occurs with time constants larger than 10 ps suggests that the electron-phonon coupling in n-types Ge/SiGe MQW structures may be less effective than that expected from the coupling constants estimated in literature and derived from bulk experiments. We are aware that a differential transmission signal has been observed in literature also after the subband population of L_1 is completely restored at its equilibrium value due to carrier heating effects [23]. In fact, an electron gas with an electronic temperature higher than the lattice one triggers a variation of the Drude absorptions of the probe signal and thus, in this regime, the decay of the differential transmission signal is governed by the redistribution of electrons in L_1 . This effect is not included in our model. However, the fact that the same set of effective OP deformation potential coefficients well reproduces the differential transmission decay in very different situations of intersubband energy separation and optical pumping power (i.e. electron temperature) suggests that this effect is not predominant in our experiments where therefore the differential transmission signal appears to be dominated by variations in the subband populations.

Finally, we remark that the presence of a less effective the electron-phonon coupling in n-types Ge/SiGe MQW structures is indeed relevant also for electrically-pumped QCL structures, even in the case the optical transition is designed well below the phonon threshold, since in QCL the electronic temperatures in the subbands is typically extremely high with respect to optically pumped devices. In the QCL design in WP 5, we will therefore take into account the possibility of lower electron-phonon couplings.

References

- [1] K. Driscoll *et al.*, Appl. Phys. Lett. **89**, 191110 (2006).
- [2] K. Driscoll *et al.*, J. Appl. Phys. **102**, 093103 (2007).
- [3] T. Grange *et al.*, Appl. Phys. Lett. **114**, 111102 (2019).
- [4] M. Virgilio *et al.*, Phys. Rev. B **86**, 205317 (2012).
- [5] J. Wang *et al.*, J. Appl. Phys. **80**, 1970 (1996).
- [6] J. Wang *et al.*, IEEE Photonics Technology Letters **8**, 1001 (1996).
- [7] M. Virgilio *et al.*, Phys. Rev. B **89**, 045311 (2014).
- [8] A. Valavanis *et al.*, Phys. Rev. B **77**, 075312 (2008).
- [9] M. Dür *et al.*, Phys. Rev. B **54**, 17794 (1996).
- [10] F. Stern *et al.*, Physical Review **163**, 816 (1967).
- [11] C. Jacoboni *et al.*, Phys. Rev. B **24**, 1014 (1981).
- [12] C. Ciano *et al.*, Physical Review Applied **11**, 014003 (2019).
- [13] M. Ortolani *et al.*, Appl. Phys. Lett. **99**, 201101 (2011).
- [14] T. Ando *et al.*, Reviews of Modern Physics **54**, 437 (1982).
- [15] H. Sakaki *et al.*, Appl. Phys. Lett. **51**, 1934 (1987).
- [16] M. Beeler *et al.*, Semicond. Sci. Technol. **28**, 074022 (2013).
- [17] I. Ezhov *et al.*, J. Appl. Phys. **119**, 033102 (2016).
- [18] D. Sabbagh *et al.*, ACS Photonics **3**, 403 (2016).
- [19] C. Ciano *et al.*, submitted to Optics Express.
- [20] M. Helm *et al.*, Phys. Rev. Lett. **63**, 74 (1989).
- [21] C. V. B. Tribuzy *et al.*, Appl. Phys. Lett. **89**, 171104 (2006).

- [22] G. Sun *et al.*, Appl. Phys. Lett. **90**, 251105 (2007).
- [23] S. Lutgen *et al.*, Phys. Rev. B **54**, R17343 (1996).